Flow, Turbulence and Combustion (2025) 115:705–738
https://doi.org/10.1007/s10494-025-00674-3

RESEARCH

High Reynolds-Number Flows Over Two Equal In-Line Rounded Square-Section Prisms at Incidence

Nils Paul van Hinsberg[1]

Received: 6 February 2025 / Accepted: 16 June 2025 / Published online: 10 July 2025

Abstract
This paper investigates the time-averaged and fluctuating aerodynamics of two slightly rough square-section prisms with rounded lateral edges of $r/D=0.16$, positioned in-line at a centre-to-centre distance $S/D=4.0$. For that purpose, distributions of the time-dependent surface pressures along both prisms' mid-span cross-sections, the derived mean sectional pressure drag, lift, and pitch moment coefficients, as well as spanwise-integrated fluctuating fluid loads on the downstream prism and the frequency of the eddy shedding in its wake were measured simultaneously for Reynolds numbers between 100,000 and 7 million. Evaluation of the data and comparison with the results of an identical single prism revealed substantial changes of the flow over both prisms with Reynolds number for all studied incidence angles between $0°$ and $45°$ in the form of mutual aerodynamic influences due to *proximity* and *wake-interference* effects. For most studied flow parameters, a good agreement of the trends of the aerodynamic coefficients with incidence angle between the upstream and reference prism are obtained. *Proximity* effects are nevertheless clearly visible in the surface pressures, particularly at $\alpha = 25.5°$. Contrarily, *wake-interference* effects lead to a much lower and even negative drag on the downstream prism. The impingement of the shear layers coming from the upstream prism or of the eddies, formed in the gap between both prisms, dominates the aerodynamics of the downstream prism. This leads not only to transitions between the adjacent *separation* and *wedge* flow regimes, as well as between the *co-shedding* and *reattachment* flow states, but also triggers the vortex shedding processes between both prisms.

Keywords Tandem prisms · Incidence angle · Reynolds number · Edge roundness · Wind tunnel · Interference effects

✉ Nils Paul van Hinsberg
nils.vanhinsberg@dlr.de

[1] Experimental Methods Department, Institute of Aerodynamics and Flow Technology, German Aerospace Center (DLR), Bunsenstrasse 10, 37073 Göttingen, Lower Saxony, Germany

1 Introduction

Across various engineering disciplines, such as civil and mechanical engineering, marine sciences, the offshore oil and natural gas exploration, or offshore wind energy, flows around structural elements with bluff square cross-sections and sharp lateral edges are commonly encountered. In the vast majority of cases, they are inherently coupled with large regions of massive, large-scale flow separation, a broad near-wake region containing highly unsteady, recirculating flow and low pressures, and eddy shedding in the wake. Consequently, these structures experience large mean drag and high fluctuating lift forces. With increasing structural height–and depth, in the case of marine applications–of modern constructions, while material usage is reduced to maintain relatively constant production costs, the resulting decrease in structural stiffness makes these structures increasingly prone to both steady and unsteady fluid dynamic effects. In such cases, the larger fluid-dynamic sensitivity often governs the critical design considerations.

To strengthen the wind and water resistance of those structures, an altering of their squared cross-sectional shapes, for example by concaving, rounding, or chamfering their lateral edges, is nowadays a common method. This passive shape modification induces an altered flow field around the structures, which leads to a refined and more stable overall surface pressure distribution. Hence, the overall fluid dynamic performance of the structures can be improved. Among the three passive flow control methods listed above, rounded edges are preferred in practical applications, mostly because of the introduction of a continuously curved and finite surface between two perpendicular side surfaces that results in superior fluid dynamic characteristics, but in various cases also owing to their more aesthetic design (Delany and Sorensen (1953) Polhamus (1958) Bokaian and Geoola (1984) James and Vogel (1996) Tamura *et al.* (1998) Tamura and Miyagi (1999) Hu *et al.* (2006) Letchford and Mason (2011) Carassale et al. (2013, 2014) Alam et al. (2020) Van Hinsberg (2024) Van Hinsberg and Frede (2025)). As a transitional geometry between sharp-edged square and fully circular cross-sections, the rounded square profile inherently exhibits flow characteristics that represent a combination of the distinct aerodynamic behaviours associated with both square prisms and circular cylinders. However, unlike sharp-edged square-section prisms, which exhibit constant fluid-dynamic properties at Reynolds numbers beyond $Re_D = 10^4$ (e.g. Bai and Mahbub Alam (2018), Van Hinsberg (2021b)), the partially rounded cross-sectional geometry introduces a–albeit limited–dependence of the fluid dynamic loading on the Reynolds-number, defined as

$$Re_{L_{ref}} = \frac{\rho U_\infty L_{ref}}{\mu} \tag{1}$$

where ρ equals the density of the fluid, U_∞ the free stream velocity, L_{ref} the reference length (i.e. the diameter or side width D of circular cylinders and squared-section prisms, respectively), and μ the dynamic viscosity of the fluid. Analogous to "infinite", i.e. two-dimensional, circular cylinders subjected to laminar or low-turbulence inflow conditions (e.g. Roshko (1961) Achenbach (1968) Schewe (1983) Niemann and Hölscher (1990), Williamson (1996) Zdravkovich (1997), Mutlu Sumer and Fredsø e (Mutlu Sumer and Fredsøe, 2006)), the transient behaviour of the locations of laminar–turbulent transition, flow separation, and shear-layer reattachment with varying Reynolds number enables the classification

of the flow over rounded square-section prisms into four distinct flow regimes, namely subcritical, critical, supercritical (including an upper transition), and transcritical. Each one of them has its specific values for the mean and fluctuating aerodynamic force coefficients and eddy-shedding frequency (Carassale et al. (2013, 2014), Van Hinsberg and Frede (2025)). Interestingly, the occurrence of large (discontinuous) changes in the fluid dynamics of circular cylinders when traversing from one flow regime to another with increasing or decreasing fluid velocity can not only be reduced, but even be tuned to an optimum by the amount of roundness of the lateral edges of square-section prisms. Moreover, the Strouhal number, being the non-dimensionlised frequency at which the eddies are shed in the wake, is reduced compared to circular cylinders. This significantly lowers the proneness to vortex-induced vibrations that result from a resonance of the shedding frequency with the natural frequency of the structure. Hence, many of the "negative" fluid dynamic characteristics associated with circular cylinders and sharp-edged square-section prisms are softened. It thereby has to be kept in mind, though, that besides the Reynolds number of the free stream the angle of incidence of rounded square-section prisms is in this case a governing parameter as well (Delany and Sorensen (1953), Polhamus (1958), James and Vogel (1996) Carassale et al. (2013, 2014) Van Hinsberg et al. (2017), Van Hinsberg and Frede (2025)).

An extensive amount of experimental and numerical research is available on the individual and combined effect of angle of incidence and lateral edge roundness on the fluid dynamics and flow topology of two-dimensional square-section prisms in cross-flows for Reynolds numbers up to 10^5 (Alam et al. (2020)). Through numerical simulation and wind tunnel experiments on the flow over a two-dimensional square-section prism with non-dimensional rounded lateral edges of $r/D = 0.167$ (wit r the dimensional edge radius) at $Re_D = 10^4$ and 10^6, Tamura et al. (1998) and Tamura and Miyagi (1999) demonstrated that at angles of incidence between $\alpha = -5°$ and $30°$ the mean drag could be reduced by values as large as 60% compared to its sharp-edged counterpart at equal incidence angle. In addition, by applying edge roundness, a decrease of the fluctuating lift by about 50% was achieved at small non-zero angles of incidence, whereas the Strouhal number increased significantly. Carassale et al. (2014) observed in their experiments on 2D square-section prisms that in the Reynolds-number range of 1.7×10^4 to 2.3×10^5 an increase of r/D from 0 to 2/15 resulted in a shift of the critical angle of incidence from $\alpha_{cr} = 12°$ to $5°$. The accompanied inversion of the slopes of the lift vs. incidence angle and drag vs. incidence angle curves, i.e. $dC_L/d\alpha$ and $dC_D/d\alpha$, respectively, from negative to positive, as well as the occurrence of the maximum Strouhal number at this specific incidence angle were attributed to the formation of a separation bubble on the lateral face exposed to the oncoming flow. Their data furthermore revealed an increase of the Strouhal number over the complete investigated range of incidence angles between $\alpha = 0°$ and $45°$.

To analyse the separated and coupled effects of variations in governing and influencing model and flow parameters (i.e. incidence angle, edge roundness, and surface roughness) on the time-resolved aerodynamics of isolated 2D circular cylinders and square-section prisms for Reynolds numbers in the range of $Re_D = 1 \times 10^5$ to 1×10^7, multiple extensive wind tunnel test campaigns were conducted by the author, the results of which have been presented and discussed in detail in Van Hinsberg (2024). Among the many different findings, the surface pressure distributions and force balance data revealed, for example, that by a gradual increase in edge roundness from $r/D = 0$ to 0.5 the curves of the mean drag and base pressure, as well as of the fluctuating lift are all shifted to lower values. The

greatest gain in reduction of each of the three aerodynamic parameters could thereby be achieved at supercritical Reynolds numbers and for increasing edge roundness values from $r/D = 0$ towards 0.16. In contrast, a further rounding of the edges of the square-section prism towards the circular cylinder case induced only small additional positive effects on the aerodynamic performance. While this study showed that the most interesting aerodynamic phenomena occur on the square-section prism with rounded edges of $r/D = 0.16$, this specific model configuration was selected to study the impact of a variation in angle of incidence between $\alpha = -45°$ and $3.25°$ on the prism's aerodynamic behaviour (Van Hinsberg and Frede (2025)). Drastic variations not only in the mean and fluctuating lift, drag, and pitch moment coefficients, but also in the Strouhal number were found at each angle of incidence. At specific combinations of Reynolds number and incidence angle, it was shown that the eddy shedding in the wake behind the prism could even be fully suppressed. Moreover, sign reversals of the lift and pitch moment coefficients were observed at the transition Reynolds numbers from one flow regime to another. By applying the linearised quasi-steady aerodynamic models to those data, the proneness to transverse and torsional galloping–two self-excited limit-cycle oscillation that arise from the motion of the vibrating prism itself– and their instability regions in terms of both Reynolds number and incidence angle could successfully be derived.

The placement of a second, identical cylindrical or sharp-edged prismatic bluff body in close vicinity of the first one, in-line with the vector of the free stream, results in most cases in a fluid-dynamic interference between the two bodies (Reinhold et al. (1977) Okajima (1979) Igarashi (1981) Pearcy et al. (1982), Igarashi (1984) Sakamoto et al. (1987), Zdravkovich (1987) Alam et al. (2002; 2003), Zhou and Yiu (2006) Sohankar (2012, 2014), Alam (2016a), Alam et al. (2016b), Du et al. (2019a, 2019b) Schewe and Jacobs (2019) Du et al. (2021), Schewe et al. (2021)). Whilst in this configuration the upstream one of the two experiences an undisturbed incoming flow, the downstream one faces a clearly altered inflow that leads to a distinct modification of the flow topology around it and thus of the instantaneous surface pressures and resultant time-mean and fluctuating fluid dynamic loads acting on it. However, depending on the proximity of both tandem bluff bodies, the fluid-dynamic alterations experienced by the downstream structure can, in turn, be communicated upstream to the second body and in that way influence its flow field as well. This results in mutual aerodynamic interferences, wherein the upstream body notices changes in the topology of, primarily, the base flow, and thus on the fluid-dynamic forces and moments. Besides the altered aerodynamics, the eddy shedding process and the flow structures in their separate or common wake are altered as well. This may give rise to the manifestation of wake-induced instabilities, such as shear-layer impingement and reattachment, quasi-periodic vortices, wake galloping, or resonance between both structures.

In contrast to the large number of studies on the flow characteristics and the ensuing aerodynamics of two 2D smooth circular cylinders or sharp-edged square-section prisms with variations in the gap size, Reynolds number, and/or angle of incidence, merely a handful of investigations are available on the fluid dynamics of a pair of inline square-section prisms with rounded edges. Among those few that focus on the combined effect of edge roundness and gap spacing, most have been performed at low to very low Reynolds numbers of $Re_D = 100$ (Adeeb et al. (2018), Datta et al. (2019), Zhang et al. (2019), Adeeb and Sohn (2021)) or $Re_D = 3 \times 10^3$ to 4×10^3 (Virkam et al. (2020)) only. The sole experimental studies on the combined effect of Reynolds number (up to 7 million) and gap size on two

identical slightly rough rounded square-section prisms with $r/D = 0.16$, positioned in-line at $\alpha = 0°$ and $45°$, were conducted by Van Hinsberg (2022). Centre-to-centre spacing ratios of $S/D = 2.8$, 4, and 5.6 between the two prisms were studied, motivated by engineering applications related to four-column deep-draft semi-submersible platforms used, for example, in the wind energy sector and the offshore oil and gas industry. All lateral faces of both models were slightly roughened to $k_s = 4.5 \times 10^{-4} D$ to simulate a light coverage by hard marine fouling often found after several years upon placement in the ocean. In Van Hinsberg (2021a), it was proven, though, that the impact of such a roughness value on the fluid-dynamic characteristics of an identical isolated prism is only marginal compared to a smooth surface. The measurements showed that the presence of the second prism in the direct wake of the upstream one induces distinct *proximity* and *wake-interference* effects between both prisms, thereby altering the flow over both at each of the two tested incidence angles. The largest influences were thereby observed on the downstream prism for which a negative drag coefficient (i.e. a thrust force) was obtained within single or multiple Reynolds-number flow regimes, particularly for $S/D = 2.8$ and 4 at $\alpha = 45°$. It was argued that the accompanied (multiple) sign switch(es) of mainly the drag force (and in a lesser extent also of the lift force and pitch moment) on the downstream prism are an indication of sharp changes in the critical spacing S/D_{cr} between both prisms with varying Reynolds number. The state of the flow around both tandem prisms thereby alternates between the *co-shedding* and the *reattachment* regimes. While with increasing gap size the fluctuating drag and Strouhal number of the downstream prism gradually approached the corresponding values for a single prism, a steady increase of the fluctuating lift over all Reynolds-number flow regimes took place at the same time, the latter indicating a growth in strength of the shed vortices compared to the isolated prism.

To further deepen the knowledge and physical understanding of how key model and flow parameters influence the mean and unsteady aerodynamic behaviour of two identical tandem prisms with rounded square cross-sections in a uniform, steady cross-flow, the wind tunnel study presented herein focuses on the combined effects of angle of incidence and Reynolds number. Based on the previously described trends of the various aerodynamic coefficients with increasing gap size, the intermediate prims-to-prism spacing of $S = 4.0D$ was chosen for the current experiment. To enable a direct comparison with the aerodynamics obtained for the single, isolated prism at incidence by Van Hinsberg and Frede (2025), the two tandem prisms had the same non-dimensional surface roughness value ($k_s/D = 4.5 \times 10^{-4}$) and lateral edge roundness ($r/D = 0.16$) as their single counterpart. Combined measurements with pressure taps and piezoelectric platform dynamometers provided (partly time-resolved, partly only time-mean) data on the cross-sectional surface pressure distribution, the base pressure, lift, drag, and pitch moment coefficients, and the Strouhal number. Both in-line prisms were studied at equal angles of incidence that were varied between $\alpha = 0°$ and $45°$ with increments of $6.5°$, in accordance with Van Hinsberg and Frede (2025). At each incidence angle, the aerodynamic characteristics of both prisms within the complete Reynolds-number range of $1 \times 10^5 \leq Re_D \leq 7 \times 10^6$ were investigated.

2 Experimental Approach

2.1 Wind Tunnel Models and Measurement Techniques

The identical wind tunnel, overall test setup, prismatic wind tunnel models, and experimental measurement techniques were used as described in detail in Van Hinsberg (2022). Therefore, only a brief overview is given below.

The two models had common side lengths of $D = 60$ mm and a span $L = 600$ mm, resulting in an aspect ratio of $AR = L/D = 10$. The lateral edges were rounded to a non-dimensional roundness value of $r/D = 0.16$ (Fig. 1), after which the complete outer surface was first carefully polished by hand before being covered with a plasmatic coating to roughen the surface to a non-dimensional equivalent sand-grain surface of $k_s/D = 4.5 \times 10^{-4} \pm 2 \times 10^{-5}$. Thirty-six pressure taps, each with a diameter of 0.3 mm, were equally distributed over the mid-span cross-section of each prism, hence, around the vertical plane at $y/D = 5$. A small relative staggering of $\Delta y/D = 0.0275$ between neighbouring pressure taps prevented the interference of the local flow over a tap hole by the wake flow generated by neighbouring ones located upstream. The time-dependent surface pressures were measured using two temperature-compensated electronic differential pressure measurement units having an accuracy of ±150 Pa (= 0.15% FS). Moreover, with the use of a dynamic calibration, an upper cut-off frequency of about 860 Hz was found for the pressure taps. The mean aerody-

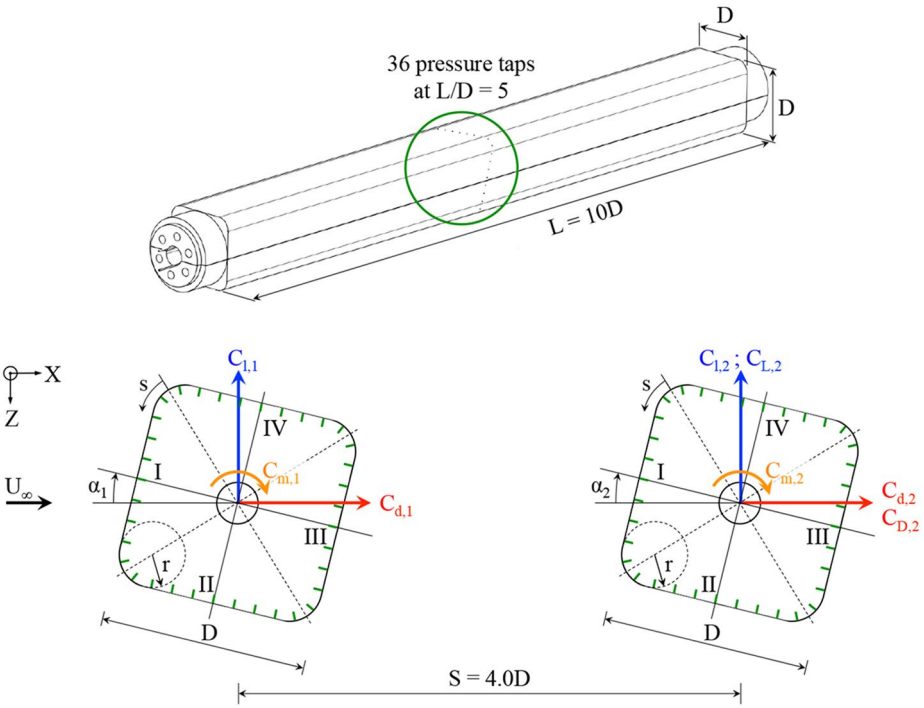

Fig. 1 Wind tunnel model geometry with locations of the staggered surface pressure taps (short green lines), definitions of the spanwise-integrated and sectional aerodynamic force and pitch moment vectors, surface coordinate s and incidence angle, and numeration of the side faces *I–IV*

namic coefficients for the drag and lift forces and the pitch moment that acted on each prism separately were calculated using those surface pressure distributions according to

$$C_{l_{1,2}} = \frac{1}{D}\int_s C_{p,cyl_{1,2}} n_Z ds = \frac{1}{D}\sum_{i=1}^{36} C_{p,cyl,i_{1,2}} n_{Z,i} ds_i \tag{2}$$

$$C_{d_{1,2}} = \frac{1}{D}\int_s C_{p,cyl_{1,2}} n_X ds = \frac{1}{D}\sum_{i=1}^{36} C_{p,cyl,i_{1,2}} n_{X,i} ds_i \tag{3}$$

$$C_{m_{1,2}} = \frac{1}{D^2}\int_s C_{p,cyl_{1,2}} n_X r ds = \frac{1}{D^2}\sum_{i=1}^{36} C_{p,cyl,i_{1,2}} n_{X,i} r_i ds_i \tag{4}$$

with $ds_i = (s_{i+1} - s_{i-1})/2$ in which s_i equals the circumferential position of pressure tap i measured along the peripheral of each prism according to Fig. 1, n the local normal vector on the prism's surface at the position of pressure tap i, X and Z the downstream and upward directed axes, respectively, with respect to the centre of the prism, r_i the distance from the longitudinal centre axis up to the position of pressure tap i of the respective prism, and $C_{p,cyl,i_{1,2}}$ the pressure coefficient at the pressure tap i, defined as $C_{p,cyl,i_{1,2}} = (p_{i_{1,2}} - p_\infty)/q_\infty$ with $p_{i_{1,2}}$ the measured static pressure at pressure tap i, p_∞ the static pressure of the free-stream flow, and q_∞ the free-stream dynamic pressure. The subscripts 1 and 2 correspond to the upstream and downstream prism, respectively. The mean base pressure coefficients $C_{pb_{1,2}}$ were obtained by taking the average of multiple mean pressure coefficients related to pressure taps located on face III (for $\alpha_{1,2}$=0°) or additionally also on face IV (for all non-zero angles of incidence). A detailed overview of the selected pressure taps used to calculate the base pressure coefficients is given in Van Hinsberg and Frede (2025).

The models were positioned in a tandem arrangement, i.e. in-line with the oncoming flow, at the centre of the test section (square cross-section of 0.6×0.6 m^2 and a length of 1 m) of the closed-circuit, low-speed High-Pressure Wind Tunnel facility of DLR. Both models thereby spanned the complete test-section width from one sidewall to the other. Because their ends passed at both sides through the sidewalls of the test section, labyrinth seals were applied to minimise the flow leakage through the small ring gaps between the wall and the model. Whereas the ends of the upstream prism were mounted directly to the outer structure of the test section, rigid piezoelectric platform dynamometers were placed between the ends of the downstream prism and the outer structure to obtain the time-dependent overall lift $L_2(t)$ and drag $D_2(t)$ forces on this prism with an uncertainty of less than 2%. The derived mean lift and drag coefficients are defined as $C_{L_2} = \overline{L_2(t)}/(q_\infty DL)$ and $C_{D_2} = \overline{D_2(t)}/(q_\infty DL)$ with $\overline{L_2(t)}$ and $\overline{D_2(t)}$ the mean values of, respectively, the time-series of the lift and drag forces. From the power spectral densities based on the fluctuations of the lift force $L_2(t)$ the main vortex shedding peaks and corresponding shedding frequencies f_{L_2} were determined. The resulting Strouhal numbers are given as $St_{L_2} = f_{L_2} D/U_\infty$.

The aerodynamics at eight angles of incidence in the range from $\alpha_{1,2} = 0°$ to 45° with an accuracy of $L/D = 10$ have been investigated for Reynolds numbers between 1×10^5 and 7×10^6. Despite a high geometric wind tunnel blockage ratio of 0.10 to 0.13, no cor-

rection for wall-interference effects has been applied to the measured aerodynamic data. Appendix A addresses this issue in more detail. At each combination of incidence angle and Reynolds number, all measurement signals were recorded over a period of 30 seconds, with a sampling frequency of $f_{scan} = 5$ kHz and a resolution of 16 bit in the case of the spanwise-integrated lift and drag forces.

2.2 Reliability Verification of the Pressure-Derived Forces

In a previous experimental study on the flow behaviour around single rounded square-section prisms with and without surface roughness in the same High-Pressure Wind Tunnel facility, surface-oil visualisations were used to examine the effect of the limited aspect ratio of $L/D = 10$ on the two-dimensionality of the flow over those prisms (Van Hinsberg et al. (2018)). It could be proven that only in a small region over the prism, which extended from each wind tunnel sidewall up to about 90% of one model diameter in spanwise direction, a three-dimensional flow over each prism was present. Since in the current study the two tandem models have both the same cross-sectional shape and dimensions, but a slightly higher surface roughness as the model on which the surface-oil visualisations were conducted, it can be argued that the flow is expected to be highly two-dimensional over a similar central section of more than 8 prism diameters in length. Because all surface pressure taps are positioned in a staggered manner around the mid-span cross-sections of the two prism, see Fig. 1, it is ensured that the pressure data–and the sectional forces and pitch moment coefficients derived therefrom–are obtained in a strictly two-dimensional flow. Only at those Reynolds numbers at which the flow gradually transits from one flow regime to another, hence, within the critical flow regime and the upper transition, it is expected that the flow field over the prism has a more three-dimensional character, similar to the circular cylinder case (e.g. Van Hinsberg (2015)).

Fig. 2 presents, exemplary for $\alpha_2 = 19.5°$, the Reynolds-number dependent time-averaged sectional and spanwise-integrated drag and lift coefficients on the downstream prism, obtained by the integration of the sectional surface through equations (3) and (2) and by the piezoelectric platform dynamometers, respectively. The similar trends of the curves and of the values of the two force coefficients for both measurement methods at most Reynolds numbers confirm the assumption of a largely two-dimensional flow along the span of the downstream prism. As expected, larger deviations between the values for both methods exist for Reynolds numbers that cover the critical flow regime up to the upper transition, which coincides with a range of approximately $3 \times 10^5 \leqslant Re_D \leqslant 5 \times 10^5$ at this specific angle of incidence.

3 Experimental Results

3.1 Time-Averaged Sectional Drag and Base Pressure Coefficients

The variations of the mean sectional pressure drag coefficients of both in-line prisms, $C_{d_{1,2}}$, and of the mean sectional base pressure coefficients, $C_{pb_{1,2}}$, with angle of incidence are illustrated in Figs. 3 and 4, respectively, for selected Reynolds numbers between $Re_D = 1.5 \times 10^5$ (i.e. subcritical) and 6.0×10^6 (hence, supercritical or transcritical,

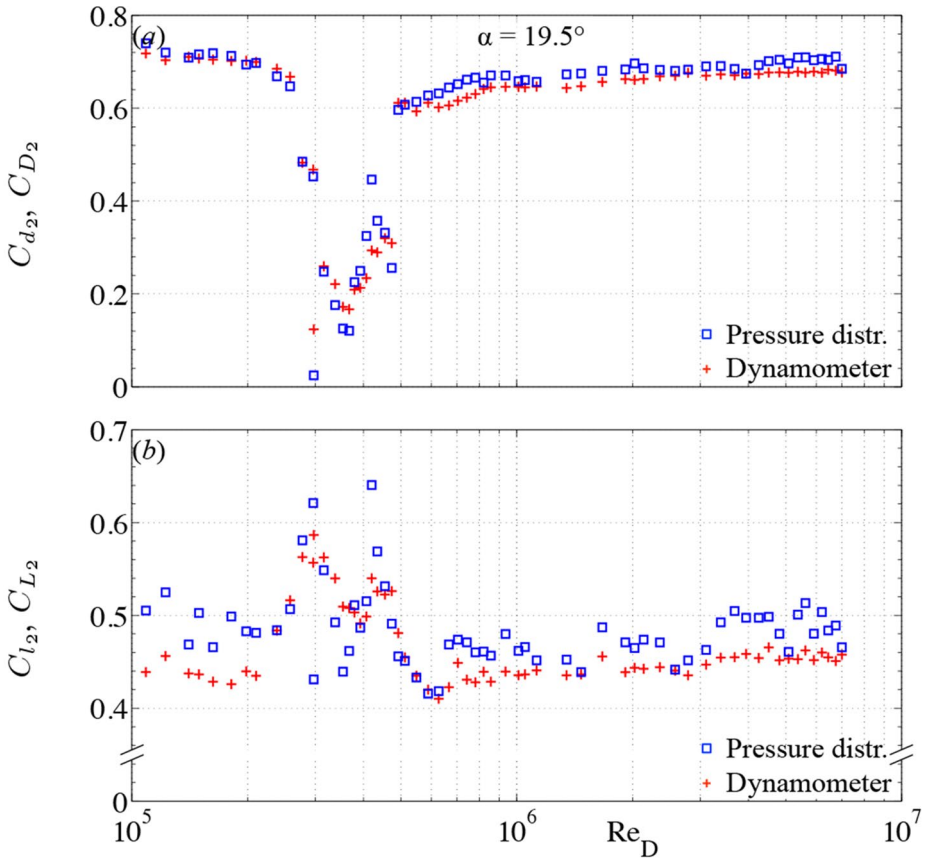

Fig. 2 Sectional and spanwise-integrated aerodynamic force coefficients, obtained by surface pressures and piezoelectric platform dynamometers, respectively, as function of the Reynolds number for the downstream tandem prism at an angle of incidence of $\alpha_2 = 19.5°$. (***a***): time-averaged drag coefficient; (***b***): time-averaged lift coefficient

dependent on the exact angle of incidence of the prisms). Both figures also include the curves of $C_d\,(\alpha)$ and $C_{pb}\,(\alpha)$, which belong to the single rounded square-section prism by Van Hinsberg and Frede (2025) that serves as reference for comparison purposes.

What probably catches the reader's eye straight away is the strong correlation between the trends of both aerodynamic coefficients with angle of incidence at all Reynolds numbers for each of the three prisms. This common behaviour is actually not that surprising, as a change in the (mean) base pressure alters the overall net (mean) pressure force that acts on the prism in flow direction. A decrease in the suction force over the prism's base surfaces thus leads to a smaller drag force, whereas an increase of the absolute base pressures induces a higher overall drag force on the prism. Although the global behaviour of the mean sectional base pressure coefficients with increasing angle of incidence is for both tandem prisms very much alike at all presented Reynolds numbers, distinct differences in the respective values for C_{d_1} and C_{d_2} are obtained. At the majority of Reynolds numbers, the drag coefficient of the upstream prism shows an gradual increase with increasing angle of incidence, in close

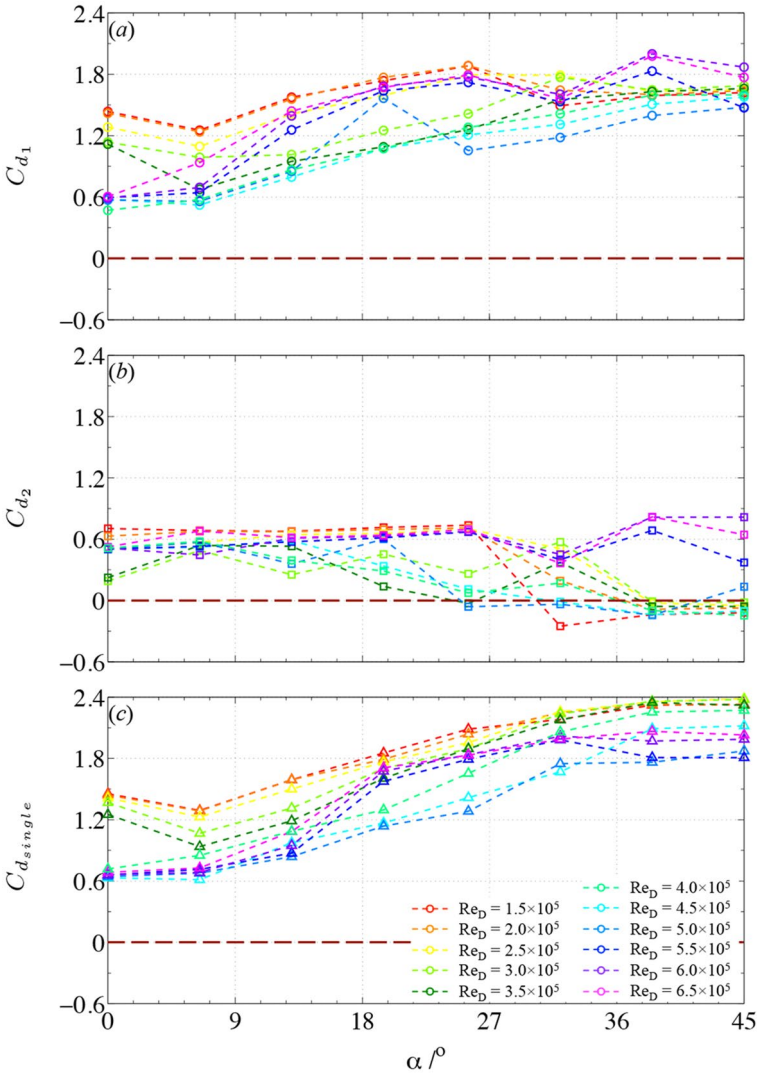

Fig. 3 Combined effects of incidence angle α and Reynolds number Re_D on the mean sectional drag coefficient. (***a***) and (***d***): upstream in-line prism; (***b***) and (***e***): downstream in-line prism; (***c***) and (***f***): isolated, identical reference prism (Van Hinsberg and Frede (2025)). First page: $Re_D = 1.5 \times 10^5 - 6.5 \times 10^5$, second page: $Re_D = 7.0 \times 10^5 - 6.0 \times 10^6$

agreement with the behaviour of $C_{d_{single}}$. For the upstream prism, a clear kink in the curves appears at $\alpha_1 = 6.5°$ for $Re_D \leqslant 3.5 \times 10^5$ (Fig. 3a), associated with the steady reattachment of the free shear layer onto side face *IV* in the vicinity of the downstream-directed rounded edge, as will be revisited in more detail in sect. 4. Since an equal value was found for the isolated prism (Van Hinsberg and Frede (2025)), the value of the critical angle of incidence seems not to be influenced by the presence of the downstream prism. At this angle of incidence, the flow state switches from the *perfect separated* flow regime to the *reattachment* or

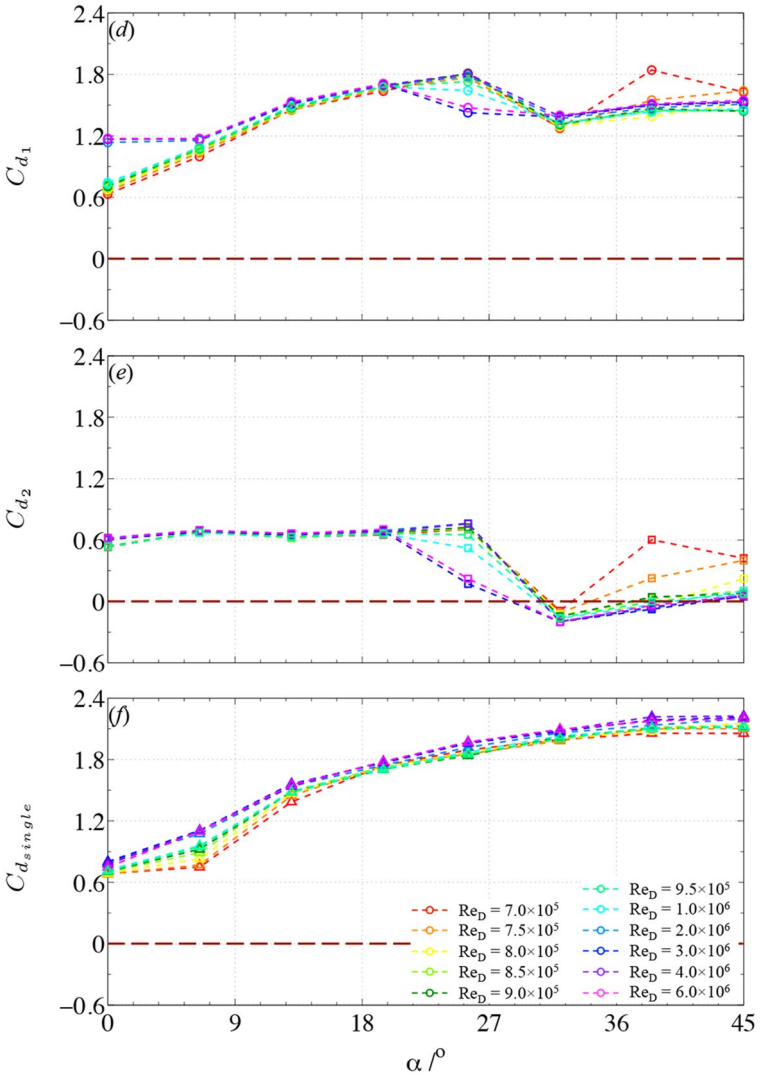

Figure 3 (continued)

separation flow regime. The conformity of the trends of $C_{d_1}(\alpha)$ and $C_{d_{single}}(\alpha)$ is actually quite remarkable, since this aspect is clearly not mirrored in the behaviour of their respective base pressure coefficients in Fig. 4, in particular at high critical and at all supercritical Reynolds numbers between apperoximately $Re_D = 3.5 \times 10^5$ and $5.0 \times 10^5 - 5.5 \times 10^5$. This implies that at those Reynolds numbers not only the pressure values at the base, but also those over the other faces of the upstream prism deviate from the values obtained for the isolated, single reference prism. This change of the overall sectional pressure distribution on the upstream prism is a clear indication for the occurrence of a mutual interference between both tandem prisms in the sense of a modification of the flow field, induced by the presence of the downstream prism, that is fed back to the upstream one as a result of the relatively close spac-

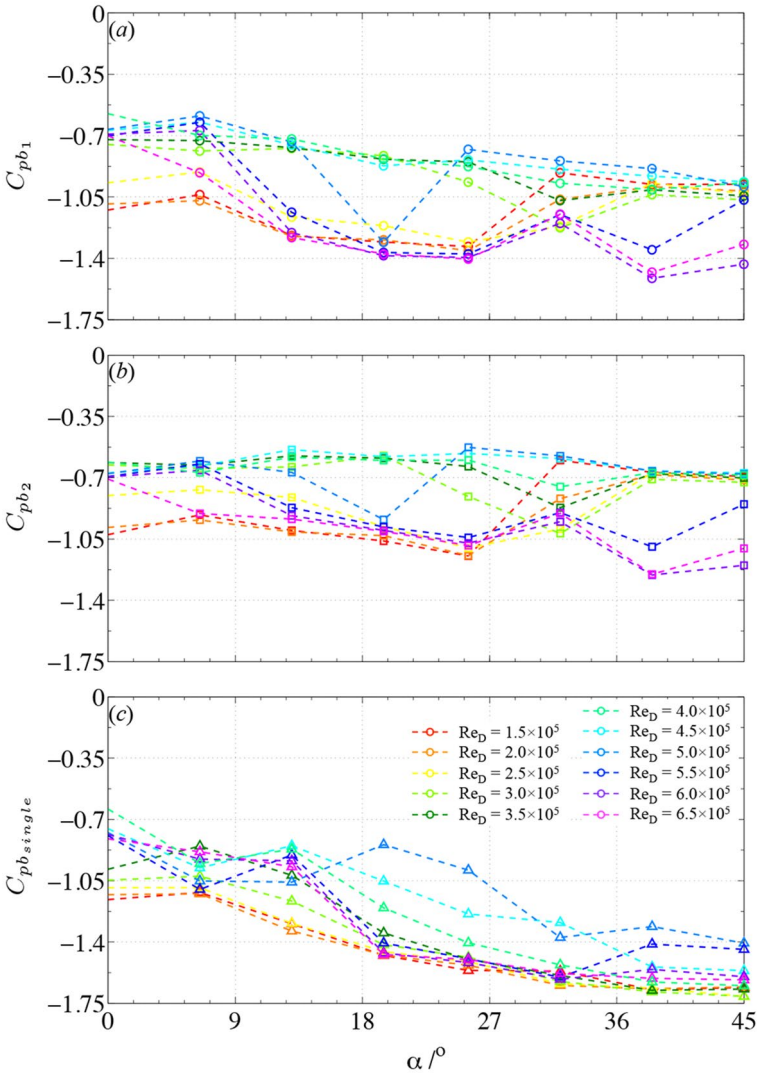

Fig. 4 Development of the base pressure coefficient with angle of incidence and Reynolds number. (***a***) and (***d***): upstream in-line prism; (***b***) and (***e***): downstream in-line prism; (***c***) and (***f***): isolated, identical reference prism (Van Hinsberg and Frede (2025)). First page: $Re_D = 1.5 \times 10^5 - 6.5 \times 10^5$, second page: $Re_D = 7.0 \times 10^5 - 6.0 \times 10^6$

ing between the two in-line prisms. It is precisely this *proximity* effect that is also responsible for the differences in both the trends and values of the drag coefficients between the upstream and the reference prism at $\alpha \geqslant 0°$ for $Re_D \geqslant 1.85 \times 10^6$ (Van Hinsberg (2022)) and for $\alpha \geqslant 25.5°$ at the majority of portrayed Reynolds numbers.

Compared to the upstream prism, the downstream one experiences significantly lower mean sectional pressure drag forces at almost all combinations of angle of incidence and Reynolds number, with the exception of a small range of supercritical Reynolds numbers between 4×10^5 and 6×10^5 at $\alpha_2 = 0°$ (Fig. 3b). For angles of incidence of $\alpha_2 = 32°$

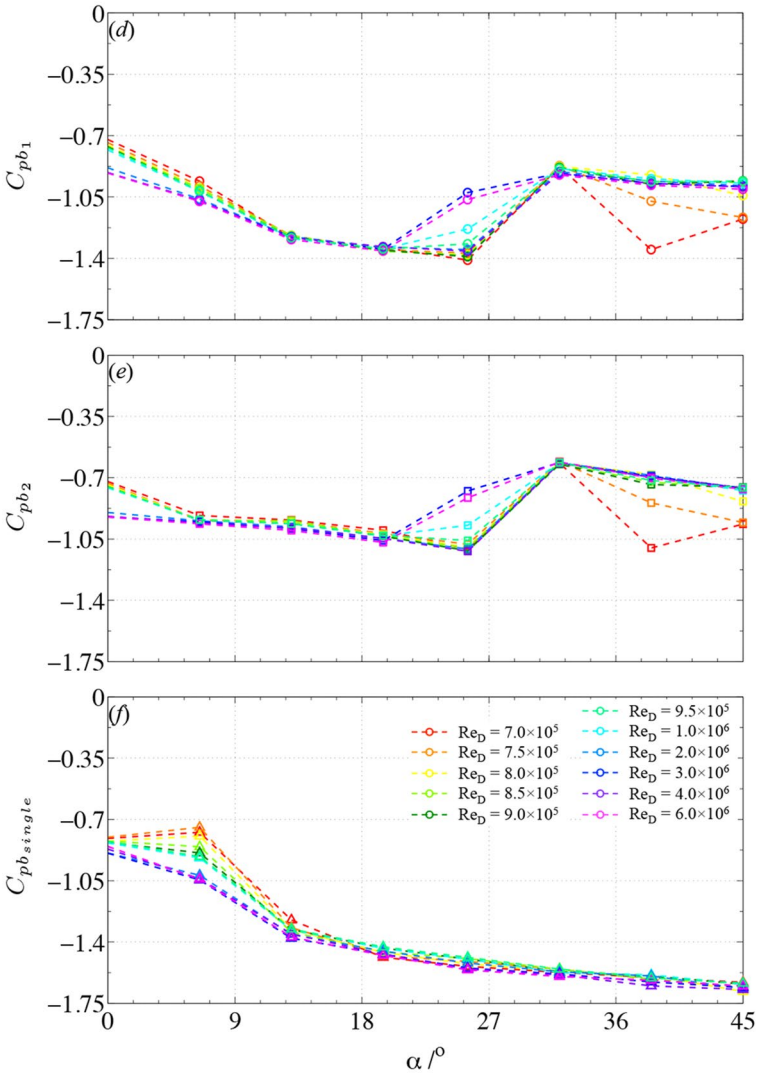

Figure 4 (continued)

and higher, even negative mean sectional drag values are obtained at certain or even at the majority of studied Reynolds numbers. Hence, at those combinations of α and Re_D the proximity of both prisms has such a strong influence on the overall flow field that the critical spacing S/D_{cr} decreases to a value below S/D, the state of the flow around the two tandem prisms thereupon switches from the *co-shedding* regime (mode *II*) to the *reattachment* (mode *I*) regime, and the downstream one of the two prisms in that way experiences a mean thrust force. In the former regime, the downstream prism is positioned sufficiently far behind the upstream one (i.e. above the critical spacing) to allow the free shear layers from the latter prism to roll up into distinct vortices in the gap between both prisms. As a result, the downstream prism experiences a periodic vortex impingement and the shed-

ding frequency of the eddies in the wake of this prism is synchronised with the periodic vortex impingement. The *reattachment* regime, on the other hand, is characterised by a reattachment of the free shear layers from the upstream prism on the downstream one. The downstream prism is thus, so to say, partially or even completely shielded from the outer flow by the wake that is enclosed by both free shear layers, whereby the amount of shielding–and thus the drag force that acts on the downstream prism–depends on the position of reattachment of the free shear layers on the side faces of the that prism. Since those free shear layers cannot roll up into distinct vortices in the gap between both prisms before their reattachment, the vortex shedding behind the upstream prism is fully suppressed and only one common Kármán vortex street is formed in the wake of the downstream prism. For $\alpha_2 \leqslant 13^\circ - 19.5^\circ$, only a relatively weak dependence of C_{d_2} on the angle of incidence is visible. At first sight, the overall lower mean drag on the downstream prism might be directly linked to the lower negative values of C_{pb_2} compared to those of the upstream prism (Fig. 4). However, the combination of a pronounced similarity in the angle-dependent behaviour of both mean base pressure coefficients at equal Reynolds number and a strong difference in the trends of the $C_d\,(\alpha)$ curves clearly infer that also on the downstream prism the overall sectional surface pressure distribution is modified substantially by the proximity of both prisms. This becomes particularly clear when comparing the trends and values of both aerodynamic coefficients for both tandem prisms for $\alpha \geqslant 32^\circ$.

3.2 Mean Sectional Lift and Pitch Moment Coefficients

The development of the mean sectional lift and pitch moment coefficient of the upstream prism (C_{l_1} and C_{m_1}) with increasing angle of incidence and Reynolds number in the Fig. 5a and 5d and in the Fig. 6a and 6d, respectively, show a good resemblance with the curves of the isolated reference prism. For Reynolds numbers beyond approximately $Re_D = 6.5 \times 10^5$, i.e. in the transcritical Reynolds-number regime, a strikingly equivalent behaviour between both prisms for the two aerodynamic coefficients is found with a strong independence on the Reynolds number. In contrast, at lower Reynolds numbers, variations in C_{l_1} (Fig. 5a) and C_{m_1} (Fig. 6a) as a result of changes in the angle of incidence appear in the form of small to moderate deviations in the trends and values between the upstream and single prism. An interesting point occurs at $Re_D = 3.5 \times 10^5$ for $\alpha = 0^\circ$ at which a high negative mean lift and positive mean pitch moment coefficient is experienced by the isolated prism, see the Figs. 5c and 6c. However, in the case of the upstream prism both aerodynamic coefficients have near to zero values instead. This significant difference between both prisms is most probably caused by a combination of the highly unsteadiness of the flow in the critical Reynolds-number flow regime, which results in strong variations in the surface pressure distribution at equal Reynolds number, and interference effects around the upstream prism induced by the direct presence of the downstream partner in its near-wake.

The downstream prism experiences at virtually all Reynolds numbers a positive mean sectional lift force and negative mean sectional pitch moment, with much smaller variations of the former and similar fluctuations of the latter with Reynolds number when compared to the upstream prism. The sharp kink in the curves at $\alpha_2 = 32^\circ$, particularly pronounced at high investigated Reynolds numbers in the Figs. 5e and 6e, is invoked by the change of the state of the flow around both in-line prisms from the *separation* to the *wedge* (or *attached*) flow regime (Van Hinsberg and Frede (2025)). Analogue to the mean sectional drag coef-

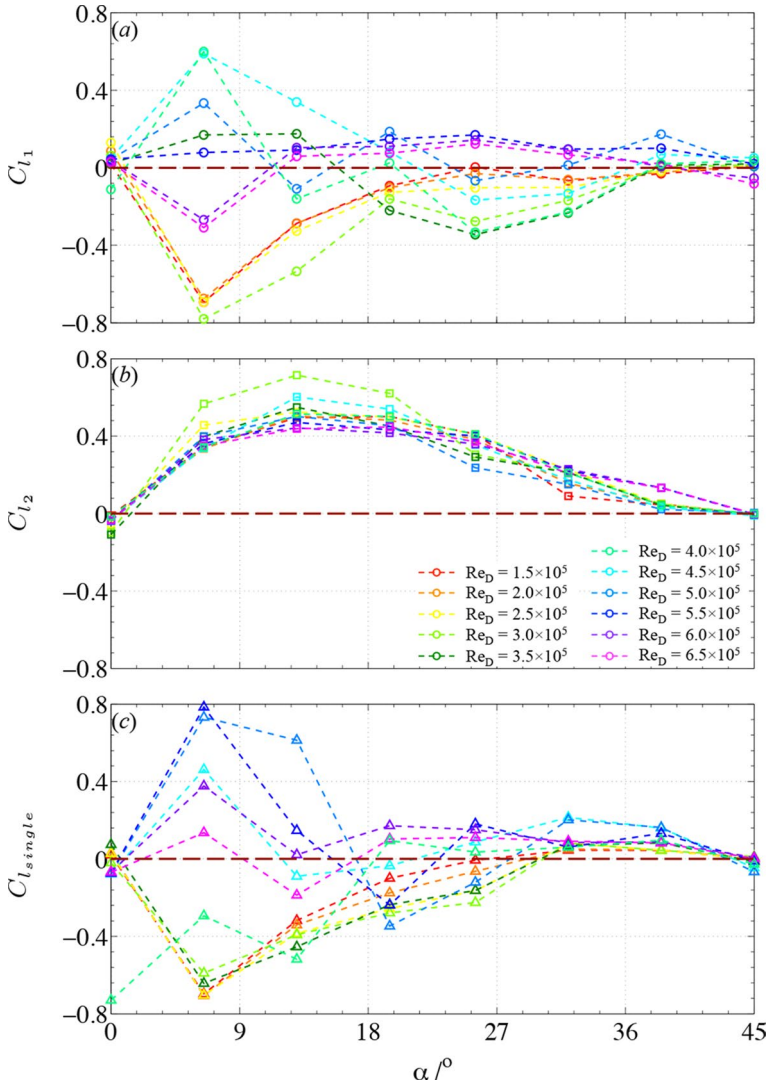

Fig. 5 Sectional lift coefficient as function of the angle of incidence and Reynolds number. (***a***) and (***d***): upstream in-line prism; (***b***) and (***e***): downstream in-line prism; (***c***) and (***f***): isolated, identical reference prism (Van Hinsberg and Frede (2025)). First page: $Re_D = 1.5 \times 10^5 - 6.5 \times 10^5$, second page: $Re_D = 7.0 \times 10^5 - 6.0 \times 10^6$

ficient in Fig. 3, this switch of the flow state is more pronounced in the aerodynamic data of the downstream prism. Hence, the proximity of the two tandem prisms apparently has a more pronounced influence on the aerodynamics of that prism, which becomes clearer when focussing on the results of the mean sectional pressure distribution in sect. 4. Interestingly, the inflection point in the curves of the mean sectional lift and pitch moment curves at $\alpha = 6.5°$, associated with the transition from the *perfect separated* to the *separation* flow regime, is then again only observed in the data of the upstream prism.

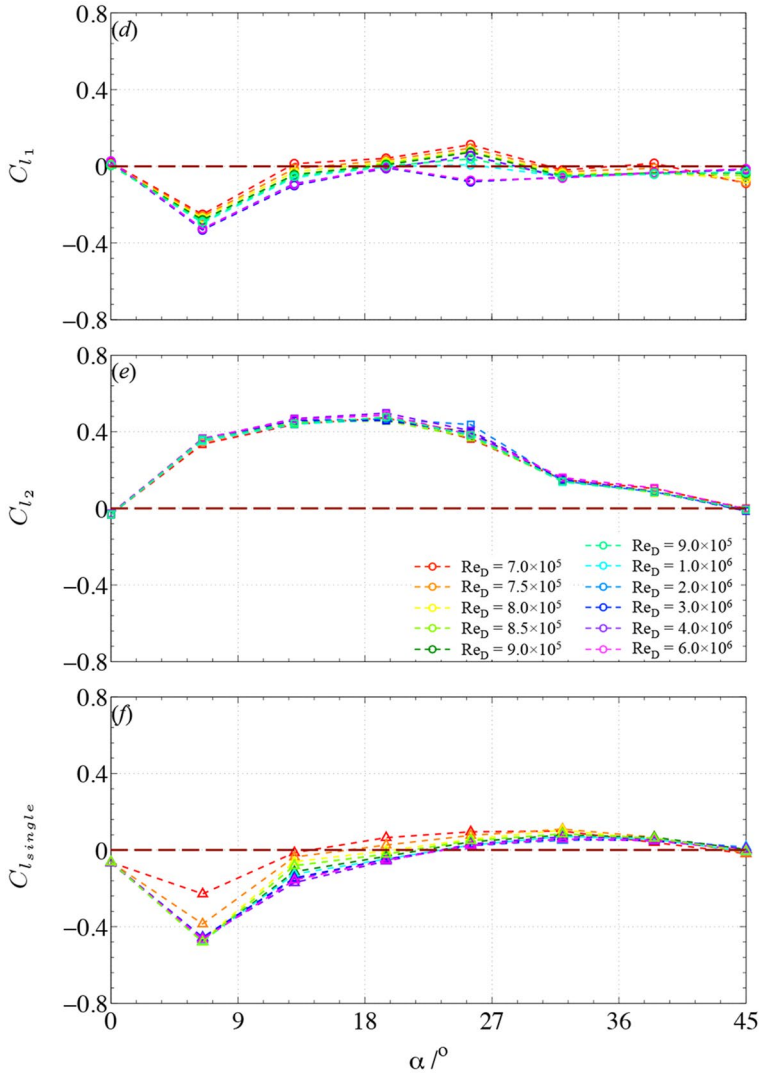

Figure 5 (continued)

Similar to the single prism configuration, distinct changes in absolute value and/or sign of the slopes of the $C_{l_{1,2}}(\alpha)$ and $C_{m_{1,2}}(\alpha)$ curves at $\alpha_{1,2} = 0°$ appear, although the two consecutive Reynolds numbers over which a switch of the sign occurs are partly slightly shifted compared to the reference prism. For the upstream prism, the sign reversals of both aerodynamic coefficients take place between $Re_D = 3 \times 10^5$ and 4×10^5 (hence, related to the transition from the critical to the supercritical flow regime) and between $Re_D = 5 \times 10^5$ and 6×10^5, i.e. connected with the crossover into the following transcritical Reynolds-number flow regime over the upper transition. In contrast, the downstream prism experiences solely one inversion from positive to negative of only the pitch moment slope at $\alpha_2 = 0°$, associated with the gradual passing from the critical to the supercritical flow regime. The

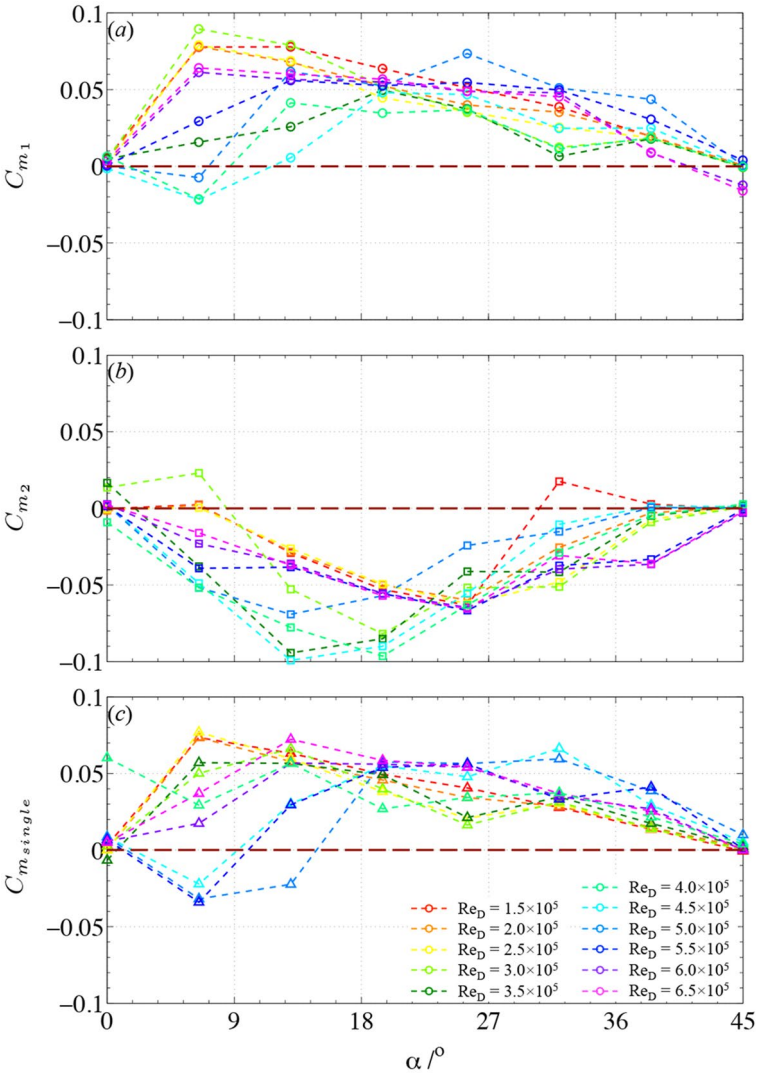

Fig. 6 Influence of the angle of incidence and Reynolds number on the sectional pitch moment coefficient. (***a***) and (***d***): upstream in-line prism; (***b***) and (***e***): downstream in-line prism; (***c***) and (***f***): isolated, identical reference prism (Van Hinsberg and Frede (2025)). First page: $Re_D = 1.5 \times 10^5 - 6.5 \times 10^5$, second page: $Re_D = 7.0 \times 10^5 - 6.0 \times 10^6$

linearised quasi-steady theory by Glauert (1919) and Den Hartog (1932) predicts a cross-over from a stable to an unstable oscillatory transverse (i.e. plunge) galloping motion round the equilibrium angle of incidence $\hat{\alpha}$ of a bluff body for cases that both the absolute value of the negative aerodynamic damping $-\{(dC_L/d\alpha)|_{\hat{\alpha}} + C_D(\hat{\alpha})\}$ exceeds the structural damping of the bluff body and the reduced velocity exceeds its critical value. Analogously, pure torsional galloping may occur when the net torsional damping $(dC_m/d\alpha)|_{\hat{\alpha}} + \zeta_\theta$ (the second term being the structural damping in torsion) is negative and perturbations in the oncoming flow induce small initial rotational oscillations of the prism round $\hat{\alpha}$. Van Hins-

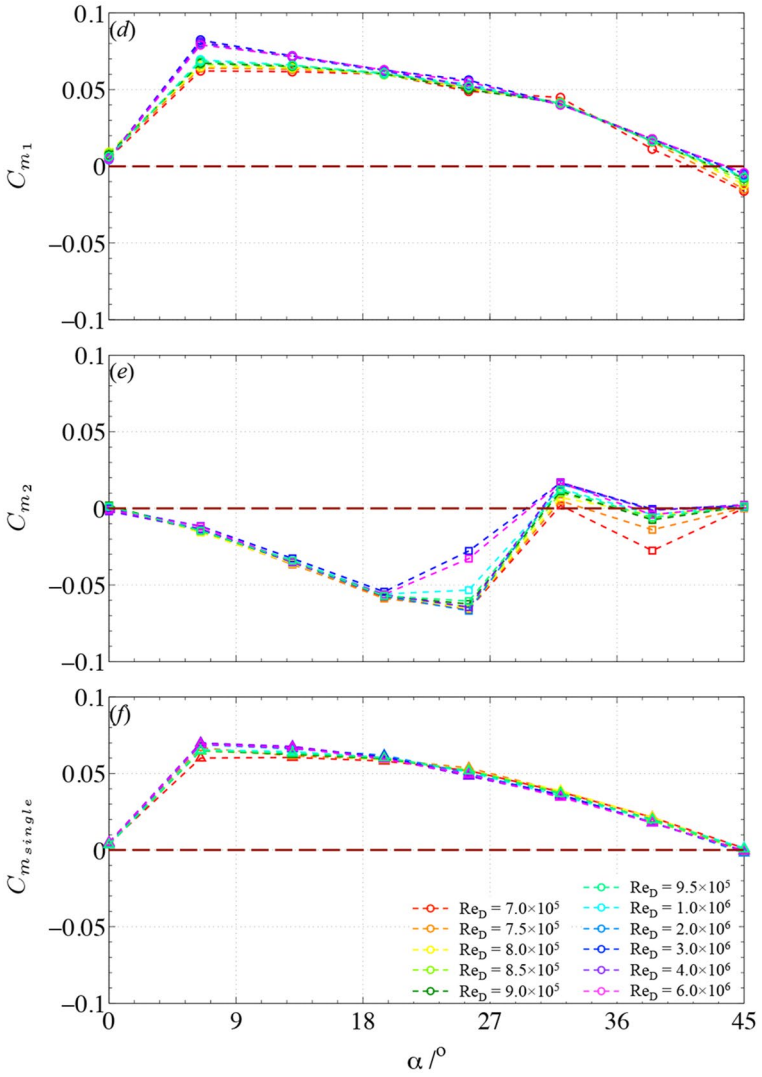

Figure 6 (continued)

berg and Frede (2025) have presented that, based on both linearised quasi-steady models, the isolated reference prism may behave as a soft oscillator to 1-DoF transverse galloping round $\hat{\alpha} = 0°$ in the limited range of Reynolds numbers bounded by $Re_D = 4.6 \times 10^5$ and 7.9×10^5, hence, only within the first part of the supercritical Reynolds-number flow regime. For the same prism, the instability regions for "soft torsional galloping" appear exactly at all other studied Reynolds numbers between 1×10^5 and 8×10^6. From the data of C_{l_1} and C_{m_1} in the Figs. 5 and 6a similar soft galloping behaviour in each of the two degrees of freedom can be derived for the upstream tandem prism, i.e. a possible tendency to pure torsional galloping over two Reynolds-number ranges that are bounded at one side only at $Re_D = 3.6 \times 10^5$ and 5.2×10^5 and an instability prone-region to 1-DoF transverse

galloping that is confined to Reynolds numbers enclosed by those two bounding values. Curiously, the downstream prism shows a possible proneness to soft transverse galloping over all Reynolds-number flow regimes. Contrarily, it has in theory only a weak susceptibility to torsional galloping at subcritical Reynolds numbers up to $Re_D = 3.5 \times 10^5$; hence, equal to the lower of the two torsional instability regions of the upstream prism.

4 Discussion

The results presented in the previous section demonstrate that, similar to the single prism case, both the Reynolds number and the angle of incidence each exert distinct influences on the aerodynamic characteristics of both tandem rounded square-section prisms. This clearly shows that both variables, i.e. Reynolds number and incidence angle, are governing parameters for the studied tandem configuration. Whereas the trends, and, at certain Reynolds numbers, even the values of the mean aerodynamic coefficients of the upstream prism with varying angle of incidence coincide quite well with those obtained for an identical single prism, substantial differences are observed when compared to the downstream prism.

Among the many interesting results, two notable findings merit closer examination, as they provide critical insights into the flow over each of the two prisms and their mutual interaction arising from *proximity* and/or *wake-interference* effects. They are associated with the transition between neighbouring angle-dependent flow regimes: in the first case from the *perfect separated* to the *separation* flow regime at the critical angle of incidence α_{cr}, whereas in the second case from the *separation* to the *wedge* flow regime. In both cases, the argumentation of the observed flow variations with Reynolds number around and at the transition angles builds thereby mainly upon the quantitative sectional distributions of the mean and fluctuating surface pressure coefficients, $C_{p,cyl_{1,2}}$ and $C'_{p,cyl_{1,2}}$, on the two prisms. Supplemental time-resolved aerodynamic data, acquired with piezoelectric platform dynamometers, reveal that the second crossover is additionally coupled with pronounced, abrupt jumps up and down in the aerodynamic loads on both tandem prisms, particularly at high Reynolds numbers exceeding $Re_D = 1 \times 10^6$.

4.1 Transition from the *Perfect Separated* to the *Separation* Flow Regime at α_{cr}

At subcritical Reynolds numbers, the flat plateau of the sectional mean and the corresponding relatively constant values of the fluctuating pressures over side faces *II* and *IV* of the upstream prism at $\alpha_1 = 0°$, displayed by the blue line in the top left image of Fig. 7 and in Fig. 8a, indicate the absence of a reattachment of the free shear layers onto these two faces. The occurrence of a mean suction peak and an adverse pressure recovery region, in combination with a narrow spike in the fluctuating pressure distribution, at first just over one and for slightly higher Reynolds numbers also over the opposite windward-directed rounded edge at $\alpha_1 = 0°$ reveals the appearance of the laminar separation bubbles over these edges. This process designates the critical flow regime in which the flow gradually transitions from the subcritical to the supercritical state. Compared to the flow field over the prism at subcritical Reynolds numbers, the current re-separation of the boundary layer over one or both rear rounded edges already at $\alpha_1 = 0°$ gives rise to a reduced interaction of both free shear layers in the gap between the two prisms (hence, smaller negative values for C_{pb_1}) and a

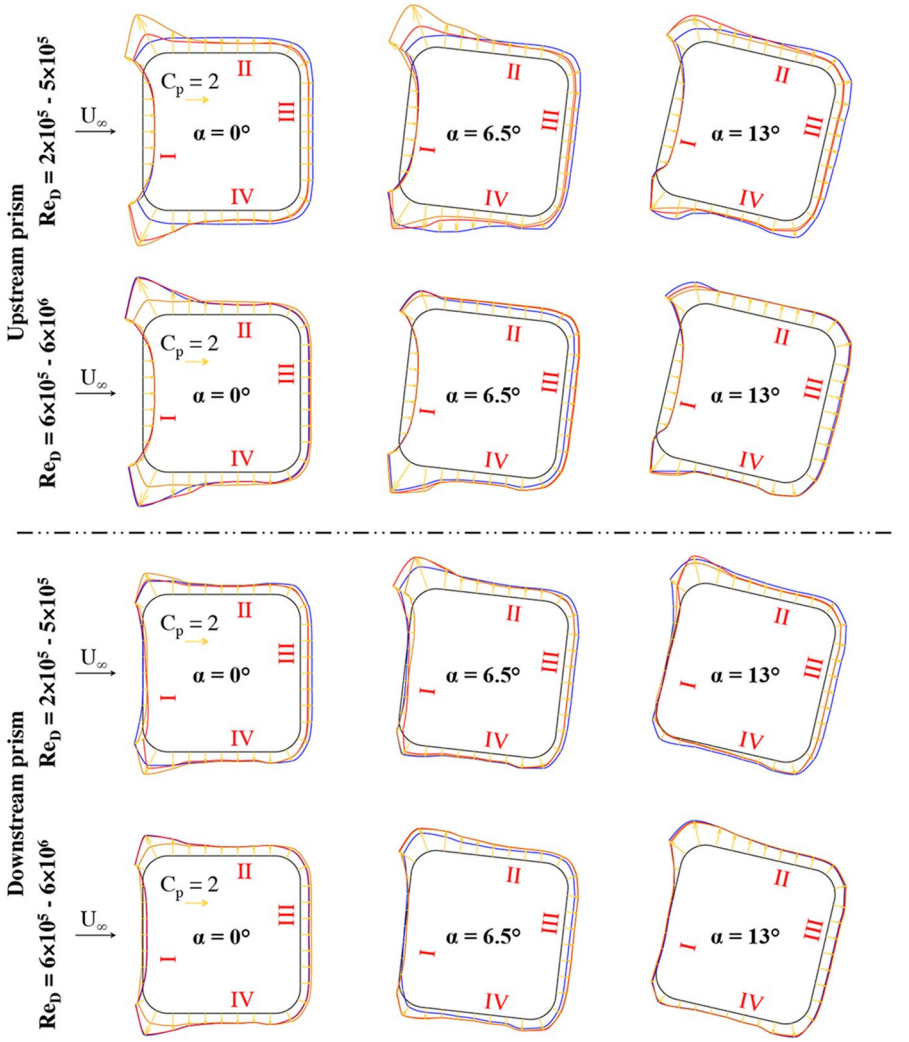

Fig. 7 Qualitative vectorial representation of the mean sectional surface pressure distributions on both tandem prisms at angles of incidence at and neighbouring the critical one for selected Reynolds numbers between $2.0 \times 10^5 - 6.0 \times 10^6$. Top two rows: upstream prism; bottom two rows: downstream prism; left column: $\alpha = 0°$; centre column: $\alpha = 6.5°$; right column: $\alpha = 13°$. 1^{st} and 3rd row: $Re_D = 2.0 \times 10^5$ (—), $Re_D = 3.5 \times 10^5$ (—), $Re_D = 5.0 \times 10^5$ (—); 2nd and 4th row: $Re_D = 6.0 \times 10^5$ (—), $Re_D = 8.0 \times 10^5$ (—)$Re_D = 6.0 \times 10^6$ (—)

smaller width of the near wake behind the upstream prism with increasing Reynolds number. The effective aerodynamic blockage thereupon decreases, which is mirrored in a gradual reduction in the mean and fluctuating surface pressures and thus the derived (sectional) drag components over the critical flow regime. A further increase in Reynolds number towards 10^7 is marked by an abrupt disappearance of the steady laminar separation bubbles and the following adverse pressure recovery regions at $Re_D = 1.85 \times 10^6$. At this point, the flow around the upstream prism switches instantly from the supercritical to the transcritical state.

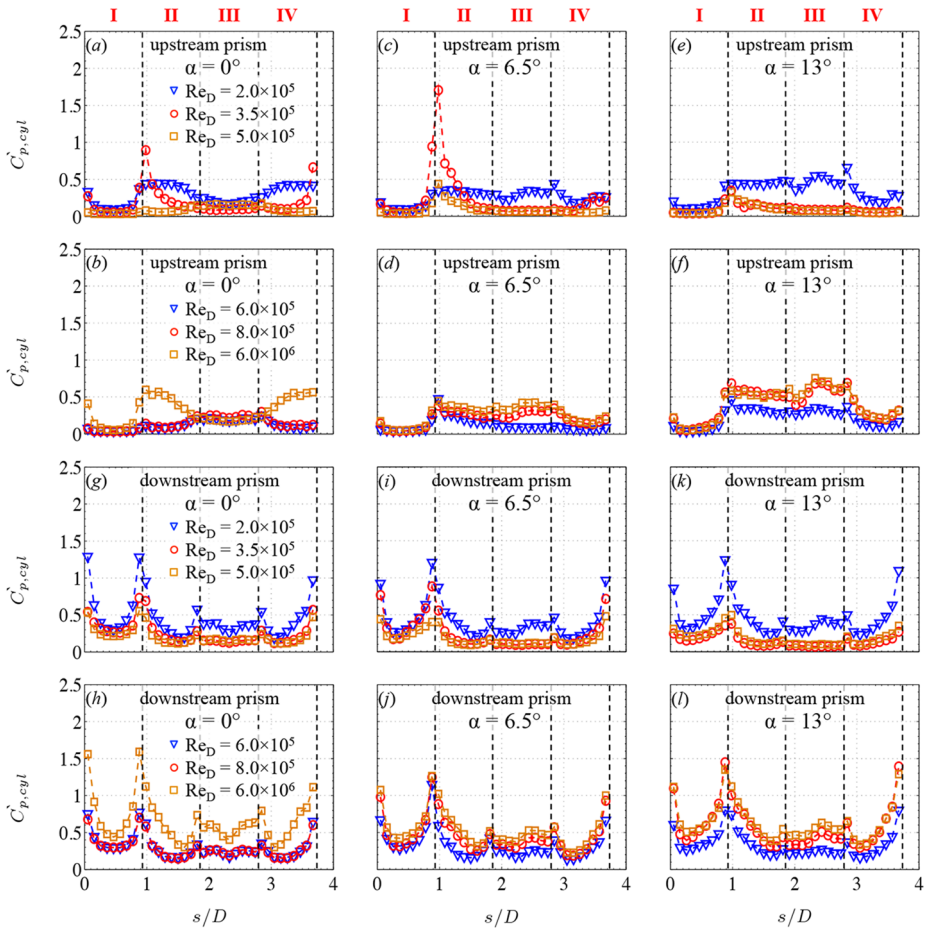

Fig. 8 Fluctuating surface pressures along the mid-span cross-section of both tandem prisms at angles of incidence in the vicinity of the critical one for six selected Reynolds numbers between $2.0 \times 10^5 - 6.0 \times 10^6$. Top two rows: upstream prism; bottom two rows: downstream prism; left column: $\alpha = 0°$; center column: $\alpha = 6.5°$; right column: $\alpha = 13°$. The colours of the curves correspond to those in Fig. 7

The sudden jump of the mean and relatively flat and small fluctuating sectional surface pressure distributions to their respective "subcritical" values (compare, for example, the blue curve in the upper left image of Fig. 7 and in Fig. 8a to the ochre-coloured curve in the left image in the second row of Fig. 7 and in Fig. 8b, respectively) explains the return of the various mean sectional aerodynamic coefficients to their subcritical levels. It sharply contrasts with the flat supercritical plateau of each of those aerodynamic coefficients (and of their fluctuating components as well) that exists up to at least the highest investigated Reynolds number of 10 million for the identical isolated prism (Van Hinsberg et al. (2017); Van Hinsberg and Frede (2025)).

The partial shielding of the downstream prism from the oncoming free stream by the relatively wide wake of the upstream prism induces a fully negative surface pressure dis-

tribution over the mid-section of the former prism at subcritical and transcritical Reynolds numbers, as illustrated in the two lower left images of Fig. 7. The strongly diminished pressures over the front face *I* due to this shielding are responsible for the significantly reduced mean sectional drag on this prism compared to its upstream counterpart in those two flow regimes. The impingement of vortical structures–produced by the process of rolling up of the free shear layers from the upstream prism in the gap between both prisms–onto the downstream prism significantly elevates the levels of pressure fluctuations over the surface of the downstream prism. At all Reynolds numbers, a separation bubble with high pressure fluctuations exists along each windward-facing edge. Hence, in contrast to the upstream prism, the free shear layers reattach to both side faces *II* and *IV* even at relatively low subcritical and critical Reynolds numbers. In supercritical flow regime, the combination of low positive mean pressure values over face *I*, induced by a reduced shielding, and the lower suction peaks over the separation bubbles in comparison to the upstream prism is mainly responsible for the occurrence of nearly equal mean drag coefficients for both tandem prisms, as presented in Fig. 3.

The crossover from the *perfect separated* to the *separation* flow regime near $\alpha_{1,2} = 6.5^\circ$ is associated with strong changes in both the mean and the fluctuating surface pressures on each of the two tandem prisms, particularly over the lower side face *IV* that is turned into the oncoming flow. At the subcritical Reynolds number of 2.0×10^5, the lower separated shear layer reattaches on the lower side face close to its trailing edge (Fig. 7). As the Reynolds number increases, the reattachment point progressively shifts upstream, leading to a gradual reduction in the size of the separation bubble, while the height of the suction peak over the lower upstream edge remains unchanged. The gradual formation of the laminar separation bubble over the upper windward-directed edge within the critical flow regime and its subsequent shrinkage, weakening, and final disappearance within the upper transition result in distinct Reynolds-number-dependent variations in the heights of the upper and lower mean negative pressure peaks. It is exactly this phenomenon that underlies the high non-zeros values and dual sign reversals of the mean lift and pitch moment coefficients, see Figs. 5 and 6. These sign changes are responsible for triggering the crossovers between stable to unstable oscillatory galloping responses–both transverse and torsional–of the upstream prism, as discussed in sect. 3.2. Figs. 8c and 8d furthermore show that at critical and supercritical Reynolds numbers a clear asymmetry in the distribution of C'_{p,cyl_1} occurs, with a maximum at $Re_D = 3.5 \times 10^5$ within the critical flow regime. The emergence of the pronounced, narrow spike over the rounded edge between faces *1* and *2* at this latter Reynolds number is most probably caused by the alternating formation and bursting of the separation bubble above this surface as the flow jumps back-and-forth between the subcritical and supercritical state.

The flow over the downstream prism exhibits at $\alpha_2 = 6.5^\circ$ similar characteristics and variations with increasing Reynolds number as those observed at $\alpha_2 = 0^\circ$. The switch from the *perfect separated* to the *separation* flow regime introduces a clear asymmetry in the "intensity" of the laminar separation bubble, though, with a much stronger bubble appearing over the upper upstream rounded edge. This gives rise to a net positive lift and negative pitch moment across nearly all Reynolds-number flow regimes (see Figs. 5 and 6). Interestingly, the difference in magnitudes of the pressure fluctuations over both edges in Fig. 8i and 8j is then again much weaker. This implies, that, similar to $\alpha_2 = 0^\circ$, the level of surface pressure fluctuations over these edges is mainly dominated by *wake-interference* effects. Apparently,

the formation of the laminar separation bubble over the upper windward-directed rounded edge of the downstream prism provokes only a weak additional fluctuation in the surface pressures, in sharp contrast to the upstream prism.

A further increase in angle of incidence within the *separation* flow regime induces a gradual decrease in both the size and strength of the laminar separation bubbles on the upstream tandem prism for Reynolds numbers that belong to the critical to upper transition flow regimes. Since these flow regimes are covered by smaller ranges of Reynolds numbers, the mean surface pressures and their derived sectional aerodynamic coefficients become successively more and more independent on variations in the Reynolds number. This growing independency is thereby more pronounced for the downstream than for the upstream prism, as exemplarily shown for $\alpha_{1,2} = 13°$ in Fig. 7. Similar to the cases at lower angles of incidence, the sectional mean and fluctuating pressure values for both prisms at transcritical Reynolds numbers largely match those observed in the subcritical flow regime, with the only notable exception occurring for the upstream prism at $\alpha_1 = 6.5°$.

4.2 Combined Switching of the Flow Regime and Flow State of Both Tandem Prisms at $\alpha_{1,2} = 25.5°$

The curve of the mean sectional drag coefficient of the upstream prism, C_{d_1}, with increasing Reynolds number at $\alpha_1 = 19.5°$ (i.e. within the separation flow regime) in Fig. 9a follows the trend of its isolated counterpart by Van Hinsberg and Frede (2025), relatively closely. Hence, relatively constant and high values at all subcritical Reynolds numbers, followed by a clear drag crisis with a steep decrease in the critical flow regime, before attaining a plateau with low values at supercritical Reynolds numbers. The subsequent large discontinuous step in C_{d_1} marks the very brief upper transition, i.e. the crossover from the supercritical to the long transcritical flow regime. This last flow regime is characterised by a flat plateau with similar values for the mean drag coefficient as those at subcritical Reynolds numbers. The only notable deviation from the single-prism configuration is that this prism exhibits a more gradual drag crisis, resulting in the subsequent supercritical flow regime collapsing onto a single Reynolds number of 5.0×10^5. Moreover, a discernible difference between C_{d_1} and $C_{d_{single}}$ is confined to the range of $Re_D = 2.3 \times 10^5$–5.0×10^5. This implies that proximity-induced interference effects–manifesting as a modification of the flow field around the upstream prism, provoked by the presence of the downstream prism and fed back to the upstream one–become apparent specifically within this Reynolds number interval, owing to the relatively close spacing between the two prisms. The distributions of the sectional mean and fluctuating surface pressures in Figs. 10, 11a, and 11b show that this mutual interference mainly alters the flow over the base of the upstream prism. The near to equal behaviour of the mean sectional drag coefficient with Reynolds number for both tandem prisms at $\alpha_{1,2} = 19.5°$ clearly confirms the existence of wake-interference effects, whereby the aerodynamics of the downstream prism is, to a large extent, controlled by the flow over and in the adjacent wake of its upstream partner. The shift of the C_{d_2} values to about half the values of C_{d_1} is thereby mainly caused by the negative pressures over the forward-directed faces I and IV–in combination with a slightly lower suction at the base compared to the upstream prism, see Fig. 4–that result from the partial shielding of this prism by the wake flow behind the upstream one. Despite this shielding of the downstream prism, a remarkable equality of its coefficients of the fluctuating drag and lift in Fig. 9b and 9c with those of the single prism are obtained. The same holds for the Strouhal number in Fig. 9c, whereby an offset to slightly lower values of St_{L_2} is found and the occurrence of two Strouhal num-

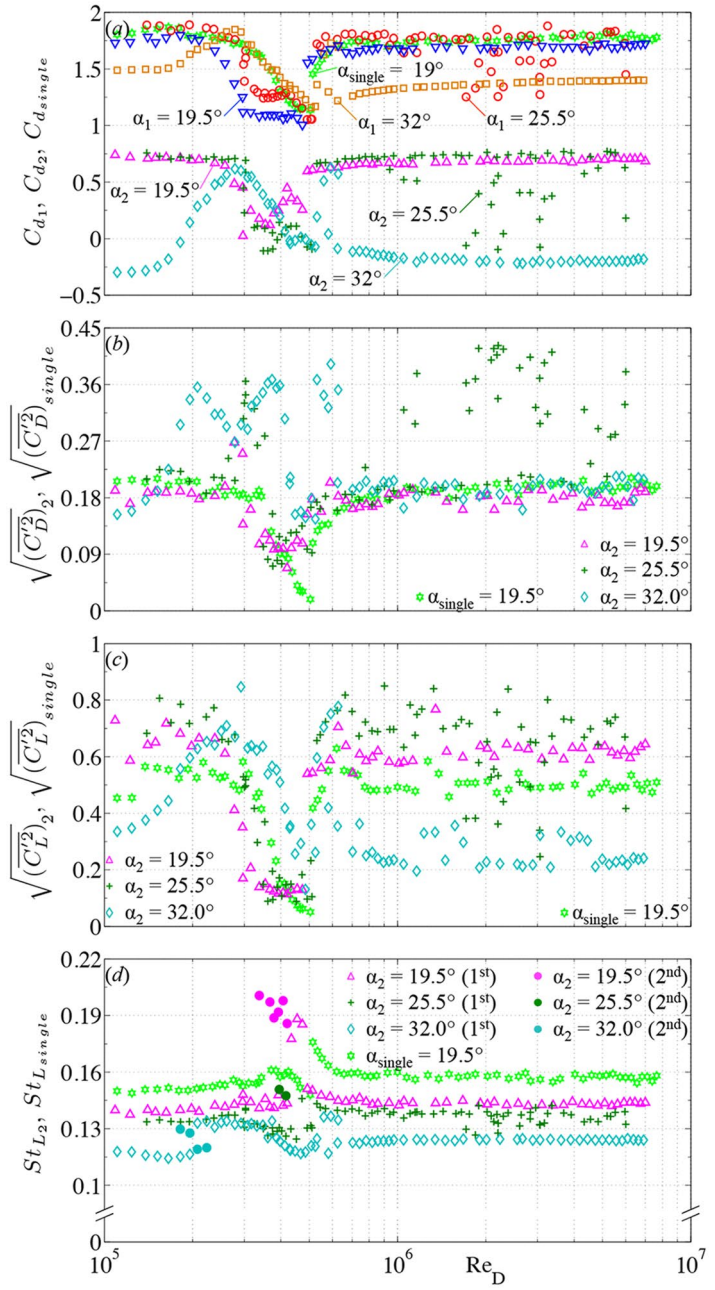

Fig. 9 Sectional mean drag coefficients on both tandem prisms, as well as the spanwise-integrated fluctuating drag and lift coefficients, and the Strouhal number of the downstream tandem prism as function of the Reynolds number for $\alpha = 19.5°, 25.5°$, and $32.0°$. For comparison, the data of the isolated, identical prism at $\alpha = 19.5°$ by Van Hinsberg and Frede (2025) are included

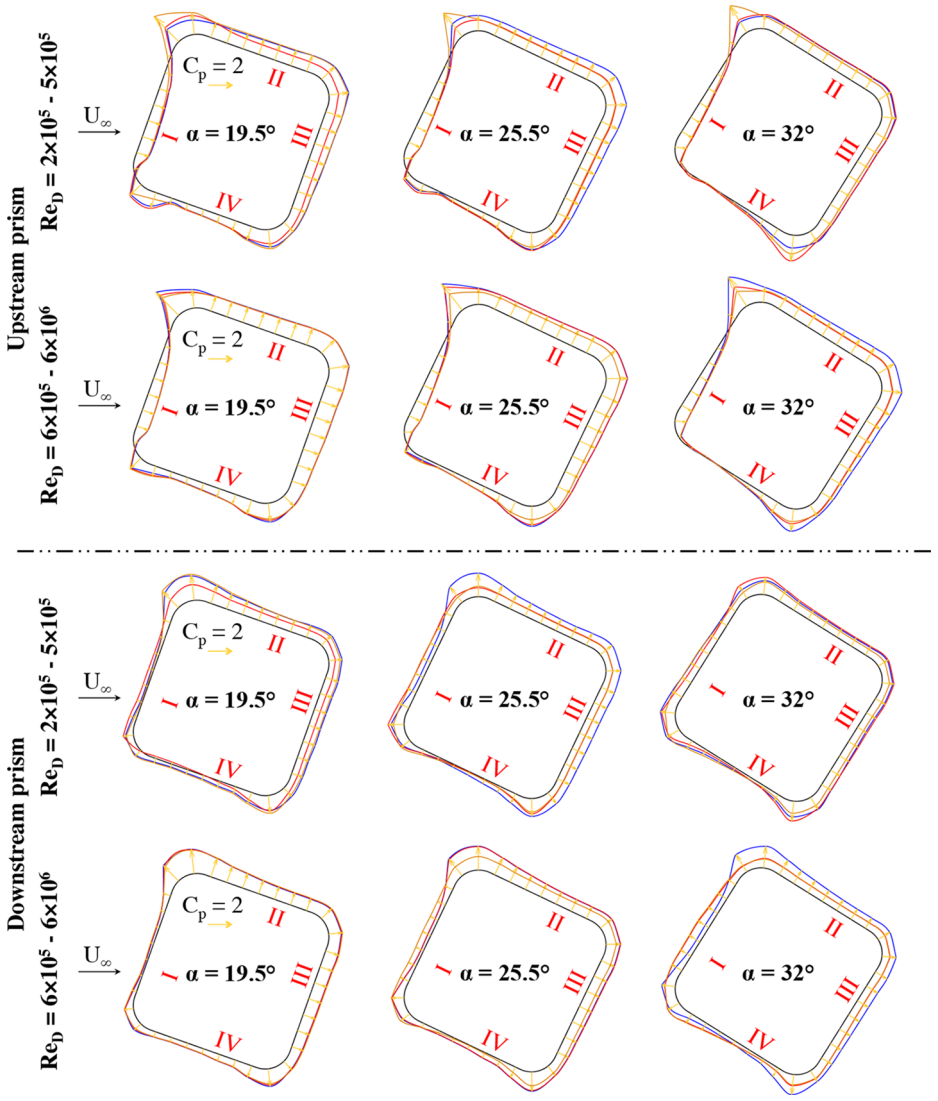

Fig. 10 Qualitative vectorial representation of the mean sectional surface pressure distributions on both tandem prisms at angles of incidence between 19.5° and for selected Reynolds numbers in the range of 2.0×10^5 to 6.0×10^6. Top two rows: upstream prism; bottom two rows: downstream prism; left column: $\alpha = 19.5^\circ$; centre column: $\alpha = 25.5^\circ$; right column: $\alpha = 32^\circ$. 1st and 3rd row: $Re_D = 2.0 \times 10^5$ (—), $Re_D = 3.5 \times 10^5$ (—), $Re_D = 5.0 \times 10^5$ (—); 2nd and 4th row: $Re_D = 6.0 \times 10^5$ (—), $Re_D = 8.0 \times 10^5$ (—), $Re_D = 6.0 \times 10^6$ (—)

bers, associated with the switching of the flow around the prism back and forth between the critical and supercritical flow states, is observed for the tandem case only. This offset most probably results from the use of the undisturbed oncoming free stream velocity U_∞ for the calculation of the Strouhal number in the tandem configuration. This velocity is expected to be slightly too high, since the downstream prism is actually exposed to the highly unsteady wake flow behind the upstream cylinder with an expected mean value of $\overline{u}_{wake} < U_\infty$ for

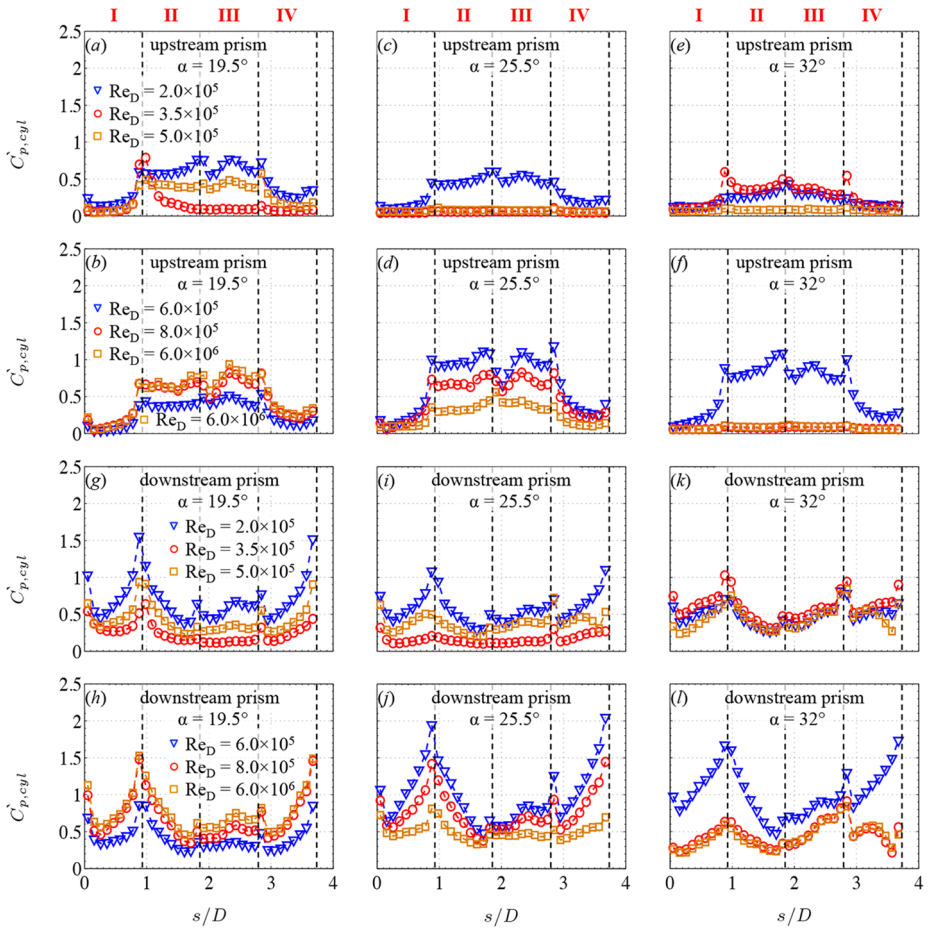

Fig. 11 Fluctuating surface pressures along the mid-span cross-section of both tandem prisms at angles of incidence between 19.5° and 32.0° for six selected Reynolds numbers ranging from 2.0×10^5 to 6.0×10^6. Top two rows: upstream prism; bottom two rows: downstream prism; left column: $\alpha = 19.5°$; centre column: $\alpha = 25.5°$; right column: $\alpha = 32°$. The colours of the curves correspond to those in Fig. 10

S/D=4.0 (Van Hinsberg (2021a)). Since $C_{d_2} > 0$ at all Reynolds numbers, the state of the flow over both prisms is part of the co-shedding regime (mode II). This implies, that the vortical structures, after detachment from the upstream prism, impinge onto the downstream prism. They thereby trigger the eddy shedding in the wake of the latter prism, which leads to a synchronisation between the shedding frequencies of both prisms (Van Hinsberg (2022)). Although the flow over the upstream prism exhibits a striking resemblance to that around the isolated prism across most flow regimes, it is nevertheless surprising that the resulting values of $\sqrt{(\overline{C_D'^2})}_2$, $\sqrt{(\overline{C_L'^2})}_2$, and St_{L_2} (and likely St_{L_1} as well) align so closely with those obtained for the single prism.

Fig. 9 illustrates that increasing the angle of incidence to $\alpha_{1,2}$=25.5° leads to several notable changes in both the trends of the curves and the corresponding values of the pre-

sented aerodynamic coefficients. These include, among others, the critical flow regime, which begins at this larger incidence angle with an extremely steep drop in $C_{d_{1,2}}$ at $Re_D = 3 \times 10^5$–hence, at the Reynolds number at which, for $\alpha_{1,2} = 19.5°$, the transition to the supercritical flow regime already takes place–to an intermediate plateau, before decreasing further to absolute minimum values at the cross-over to the supercritical flow regime. Both stages comprise a narrow Reynolds number range in which C_{d_2} becomes negative, signifying a temporary switch from the *co-shedding* (mode *II*) to the *reattachment* (mode *I*) regime. The crossovers from one mode to the other are attributed to an enhanced shielding of this prism from the oncoming free stream by the reattachment of the free shear layers after separation from the upstream prism. The exceptionally low and flat profiles of the sectional pressure fluctuations over the base of the upstream prism in Fig. 11c, and to a lesser extent also over both windward-directed faces of the downstream prism (Fig. 11i), are evidence of the presence of a practically stagnant flow that is enclosed by these shear layers and both tandem prisms. It creates a constant suction over face *I* of the downstream prism that corresponds to the negative pressures on the base face *III* of the upstream prism, as seen in Fig. 10, which is predominantly responsible for the measured thrust force. In contrast, the steep drag crisis at $Re_D = 3 \times 10^5$ is accompanied with abrupt jumps up an down in C_{L_2} and C_{D_2} as the flow around the downstream prism transitions between the subcritical and critical state. This leads to a marked increase in the fluctuating aerodynamic forces on that prism, while the shedding frequency of the eddies in its wake remains only marginally affected (Fig. 9).

The most striking observation, though, is the emergence of immense variations in all mean and fluctuating aerodynamic coefficients of both in-line prisms within the transcritical flow regime for Reynolds number exceeding approximately 1 million, which are not appearing in the single prism configuration. By comparing, for example, the non-dimensionalised time series of the spanwise-integrated drag coefficient at $Re_D = 1.84 \times 10^6$ in Fig. 12b with those measured at $\alpha_2 = 19.5°$ (Fig. 12c) and $\alpha_2 = 32.0°$ (Fig. 12d), it can be deduced that the flow over both prisms intermittently switches between the characteristic flow fields associated with the *separation* (at $\alpha°$) and *wedge* (at $\alpha_{1,2} = 32.0°$) flow regimes, respectively, in close agreement to the flow behaviour of the single prism. This is confirmed by the distribution of the sectional mean and fluctuating surface pressures at $Re_D = 6 \times 10^6$ shown in Figs. 10 and 11, where the values of $C_{p,cyl_{1,2}}$ and $C'_{p,cyl_{1,2}}$ at $\alpha_{1,2} = 25.5°$ fall between those obtained for $\alpha_{1,2} = 19.5°$ and $32.0°$. Moreover, the hops between positive and negative mean drag coefficients on the downstream prism at $\alpha_2 = 25.5°$ in Fig. 12b prove that not only the flow regime, but at the same instant also the state of the flow over both prisms jumps between the *co-shedding* (i.e. positive drag) and the *reattachment* (negative drag) regimes. Large variations in the shielding of the downstream prism thus occur, which indicates the presence of strong temporal flow changes in the gap between both prisms. Those latter changes are also visible in the time series of the spanwise-integrated lift coefficient of the downstream prism, Fig. 12a. The large fluctuations in C_{L_2}–and in C_{D_2} as well, see Fig. 9b–are attributed to the impingement of the vortical structures on the downstream prism in the *co-shedding* flow regime. In contrast, in the *reattachment* flow regime, the reattachment of the free shear layers from the upstream prism to the downstream one leads to a more stable flow and consequently reduced force fluctuations on that prism. As a final noteworthy remark, an unstable flow situation can also be identified for $\alpha_{1,2} = 32.0°$ within the narrow Reynolds-number range of approximately 5×10^5 to 7×10^5. Also in this case alternates the

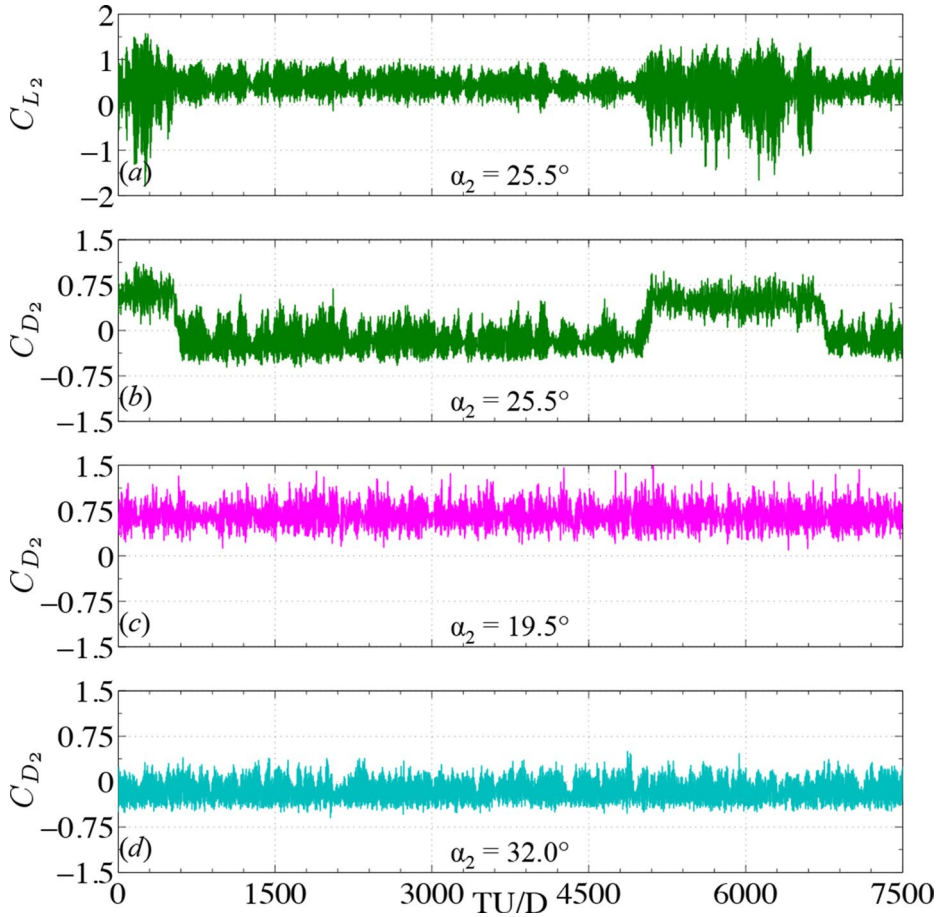

Fig. 12 Non-dimensionalised time series of the spanwise-integrated lift and drag coefficients on the downstream prism at various incidence angles within the transcritical flow regime. (**a**) and (**b**): C_{L_2} and C_{D_2} at $\alpha_2 = 25.5°$ for $Re_D = 1.84 \times 10^6$; (**c**): C_{D_2} at $\alpha_2 = 19.5°$ for $Re_D = 1.91 \times 10^6$; (**d**): C_{D_2} at $\alpha_2 = 32.0°$ for $Re_D = 1.90 \times 10^6$. The colours of the curves correspond to those in Fig. 9

flow over both prisms between the combined *separation* and *co-shedding* (mode *II*) flow regimes on one hand, and the *wedge* and *reattachment* (mode *I*) flow regimes on the other. This transitional behaviour is substantiated by the strong similarity in both the mean and fluctuating surface pressure distributions observed at $\alpha_{1,2}$=25.5° and 32.0°, exemplified at Re_D=6×10^5 in Figs. 10 and 11.

5 Conclusion

The aerodynamics of two identical 2D prisms with rounded square cross-sections, arranged in a tandem configuration at a centre-to-centre distance of $S/D = 4.0$, have been systematically examined through an extensive wind-tunnel measurement campaign. Two governing model and flow parameters, i.e. the Reynolds number of the free stream and

the angle of incidence of both prisms, were varied independently over a large range: $1 \times 10^5 \leq Re_D \leq 7 \times 10^6$ —hence, covering all possible Reynolds-number flow regimes from subcritical up to transcritical—and $\alpha_{1,2} = 0°$ to $45°$ in steps of $6.5°$. The focus was thereby placed on the trends and values of the mid-section surface pressure distributions and their derived sectional coefficients (base pressure, lift, drag, and pitch moment), as well as on the spanwise-integrated time-dependent fluid forces experienced by the downstream prism and the shedding frequency of the eddies in its wake. Their analysis and comparison to the experimental data by Van Hinsberg and Frede (2025) of the identical isolated reference prism have revealed that variations of both key parameters have a distinct impact on the flow around the two prisms, in the form of mutual aerodynamic influences induced by *proximity* and *wake-interference* effects.

The trends of the mean sectional aerodynamic coefficients with increasing angle of incidence equal at the majority of studied Reynolds numbers to a large extent those of the single reference prism. This also counts for the value of the critical angle of incidence at which the flow switches from the *perfect separated* to the *separation* flow regime, which is found to be situated in both cases at or in close vicinity of $\alpha_{1,2} = 6.5°$; hence, a reduction of α_{cr} by about 50% in comparison to the sharp-edged counterpart. This crossover is accompanied with several sign switches in both the lift and pitch moment with increasing Reynolds number for the upstream prism only. By applying the classical linearised 1-DoF transverse and rotational galloping models to those data, it could be demonstrated that, in theory, both in-line prisms possess instability regions at $0°$ angle of incidence in which either one of the two galloping modes becomes possible. Hence, consistent with the results of the single reference prism (Van Hinsberg and Frede (2025)), both rounded square-section prisms can be designated as soft oscillators within specific (one-side bounded) Reynolds-number ranges.

Pronounced effects of *proximity* and *wake interference*, arising from mutual flow interactions between the two prisms owing to their relatively close spacing, become particularly evident around $\alpha_{1,2} = 25.5°$. At specific Reynolds numbers that belong to the critical or transcritical flow regimes large variations in all aerodynamic coefficients of both prisms emerge, which are not appearing in the single prism configuration. They are caused by large variations in the shielding of the downstream prism by the wake of the upstream one as the flow temporally jumps into the combined *wedge* and *reattachment* flow regimes, associated with the flow state around both tandem prisms at the higher angle of incidence of $32°$, before returning, for a short time, to the combined *separation* and *co-shedding* flow states. This results in distinct temporal flow changes in the gap between both prisms, mirrored in altered distributions of the mean and fluctuating surface pressures on the downstream prism. By a feedback mechanism, the flow over the upstream prism is thereupon indirectly modified as well, primarily noticeable by changes in the pressures over its base surface and thus in the resultant pressure drag.

Appendix A. On the Correction of the Geometric Wind Tunnel Blockage

A high geometric wind tunnel blockage ratio, as is the case in the current study with values between 10% and 13% for $\alpha_{1,2} = 0°$ up to $45°$, and an even higher resultant effective aerodynamic blockage due to the lateral spreading of the free shear layers above the side faces and in the near wake of both prisms causes a local acceleration of the flow around the

two models, the so-called wind-tunnel wall interference effect. Since the values of the raw aerodynamic data are directly linked to that higher flow velocity, they generally have to be corrected to values that coincide with "free flow conditions", i.e. without the wind tunnel walls that restrict the flow field around the models.

In the current investigation, though, no such correction method has been applied. This decision was made for the following reasons. Most notably, it remains ambiguous–particularly for the downstream prism–which reference value of the mean flow velocity should be used as the basis for applying such a correction. While for the upstream prism the mean velocity of the undisturbed oncoming flow U_∞ can be used, the downstream prism still experiences for $S/D = 4$ a highly turbulent oncoming flow with a mean value that is lower than that for the upstream prism because of the velocity defect in the near wake behind the latter prism. Using U_∞ for the downstream prism as well would then again result in an a priori unknown over-correction and thus a certain falsification of the measured aerodynamic data for the downstream prism. Additional measurements using techniques like Particle Image Velocimetry (PIV), Laser Doppler Anemometry (LDA), and Hot-Wire Anemometry (HWA), or numerical simulations could give the necessary information on the velocity field both in the gap between the two prisms and over the downstream prism, from which the required correction for the geometric blockage could be derived. However, those measurements and CFD calculations are out of the scope of the current experimental study. Second, the solid-blockage correction formulas by Allen and Vincenti (1944) and Roshko (1961), generally applied by the author in experimental studies on single rounded square-section prismatic bluff bodies to correct the measured free-stream velocity, spanwise-integrated overall drag force, and surface pressure coefficients, are actually known to be inaccurate within the critical flow regime and the upper transition. These equations were namely originally validated against aerodynamic data at relatively low Reynolds numbers belonging to the subcritical flow regime. They therefore do not take into account the strong variations of the positions of the boundary-layer separation points over the curved edge surfaces of such prisms and the near-wake structure that occur at higher Reynolds numbers up to transcritical ones. The author is not aware of any references to date in which modifications of these equations are presented for isolated (rounded) square-section prisms, let alone for two inline ones.

In that context, the omission of a geometric blockage correction method in this publication may furthermore raise the question of the quantitative reliability and validity of the aerodynamic data presented, especially with regard to its potential use for comparison with experimental data by others and for CFD validation purposes. In Van Hinsberg (2021b), the aerodynamic data of a single 2D sharp-edged square-section prism have been presented, obtained in the same wind tunnel facility and at equal boundary conditions (hence, measurement techniques, aspect ratio and cross-sectional lengths of the model, and turbulence intensity of the oncoming flow) as the data presented in the current study. A comparison of the mean aerodynamic force coefficients and the Strouhal number of the sharp-edged prism at $\alpha = 0°$, $22.5°$, and $45°$, obtained in the High-Pressure Wind Tunnel facility, to the values obtained by Carassale et al. (2014), as their aerodynamic data and in particular the Strouhal number were acquired with piezoelectric platform dynamometers as well, revealed only marginal differences of less than 3% between both experimental studies. Note, that the former data were corrected for the geometric wind tunnel blockage of 10% (for $\alpha = 0°$) to 13% (at $\alpha = 45°$) using the formulas by Allen and Vincenti (1944) and by Roshko (1961),

$$U_{corr} = U_{uncorr}(1 + 0.25C_{D,uncorr}\frac{A}{Z_{wt}} + 0.85(\frac{A}{Z_{wt}})^2) \tag{5}$$

$$C_{p,corr} = (C_{p,uncorr} - 1)(\frac{U_{uncorr}}{U_{corr}})^2 + 1 \tag{6}$$

where A equals the area of the prism subject to the flow and Z_{wt} the height of the test section at the location of the model. In contrast, no solid blockage correction was applied to the data presented by Carassale et al. (2014). In addition, the difference in Reynolds number, hence, $Re_D = 3.7 \times 10^4$ (Carassale et al. (2014)) compared to $10^5 \leq Re_D \leq 10^7$ (Van Hinsberg (2021b)), has no influence on the values of the aerodynamic coefficients and can thus be ignored, since for $Re_D \geq 10^4$ the flow around the sharp-edged square-section prisms is situated in the *shear layer transition II* regime and is thus highly Reynolds-number independent (Bai and Mahbub Alam (2018), Van Hinsberg (2024)). In the case we now apply a retrospective correction to the data by Carassale et al. (2014) for their geometric wind tunnel blockage ratio of only 2.5% at $Re_D = 3.7 \times 10^4$, the difference in the aerodynamic values between both experimental studies reduces to merely 1%. This high degree of equality in the values of the aerodynamic coefficients, upon correction for the–completely different–geometric wind tunnel blockage ratios, clearly implies the validity of the obtained values for the various aerodynamic coefficients in the current wind tunnel facility, even in the case of high solid blockage ratios. Moreover, for 2D square-section prisms the flow field around the sharp-edged configuration is characterised by the highest lateral spread of the free shear layers along both side faces and in the near wake, which thus leads to the largest possible effective aerodynamic blockage. A rounding of the lateral edges of the model lowers this aerodynamic blockage, while the solid blockage is only merely altered.

Although the correction method described above leads to meaningful and credible results in the case of isolated square-section prisms, the author has nevertheless decided against applying this correction method to both in-line rounded square-section prisms for the reasons mentioned at the beginning of this section. Readers are nevertheless free to apply equations (5) and (6) or any other correction method to the current data for comparison with their own experimentally or numerically obtained results.

Acknowledgements Technical assistance of Markus Löhr of the DLR Institute of Aeroelasticity and Karsten Steiner of DNW is gratefully acknowledged. DLR Systemhaus Technik and Deharde are recognised for the construction and manufacturing of the wind tunnel models, respectively.

Author Contributions The author confirms sole responsibility for: study conception and design, data collection, analysis and interpretation of results, manuscript writing, and project administration.

Funding Open Access funding enabled and organized by Projekt DEAL. The author declares that he did not receive any funding to carry out the present study.

Data Availability The data that support the findings of this study are available upon reasonable request.

Declarations

Conflict of Interest The author declares no competing interests.

References

Alam MM, Abdelhamid T, Sohankar A.: Effect of cylinder corner radius and attack angle on heat transfer and flow topology. Int. J. Mech. Sci. **175**. 105566–114 (2020). https://doi.org/10.1016/j.ijmecsci.2020.105566

Alam MM, Bai H, Zhou Y.: The wake of two staggered square cylinders. J. Fluid Mech. **801**. 475–507 (2016a). https://doi.org/10.1017/jfm.2016.303

Achenbach E.: Distribution of local pressure and skin friction in cross flow around a circular cylinder up to. J. Fluid Mech. **34**. 625–639 (1968). https://doi.org/10.1017/S0022112068002120

Adeeb E, Haider BA, Sohn CH.: Influence of rounded corners on flow interference between two tandem cylinders using fvm and ib-lbm. Int. J. Heat Fluid Flow. **28**. 1648–1663 (2018). https://doi.org/10.1108/HFF-08-2017-0319

Alam MM.: Lift forces induced by the phase lag between the vortex sheddings from two tandem bluff bodies. J. Fluids Struct. **65**. 217–237 (2016b). https://doi.org/10.1016/j.jfluidstructs.2016.05.008

Alam MM, Moriya M, Takai K, Sakamoto H.: Suppression of fluid forces acting on two square prisms in a tandem arrangement by passive control of flow. J. Fluids Struct. **16**. 1073–1092 (2002). https://doi.org/10.1006/jfls.2002.0458

Alam MM, Moriya M, Takai K, Sakamoto H.: Fluctuating fluid forces acting on two circular cylinders in a tandem arrangement at a subcritical reynolds number. J. Wind Eng. Ind. Aerod. **91**. 139–154 (2003). https://doi.org/10.1016/S0167-6105(02)00341-0

Adeeb E, Sohn CH.: Flow and heat transfer characteristics of cylindrical structures with corner radius variation: tandem, side-by-side, and flow-induced vibration. Heat Transf. Eng. **42**. 251–269 (2021). https://doi.org/10.1080/01457632.2019.1699293

Allen HJ, Vincenti WG.: Wall interference in a two-dimensional flow wind tunnel with consideration of the effect of compressibility. Nat. Adv. Comm. Aero. Technical Report (1944). Technical Report 782

Bokaian AR, Geoola F.: Hydroelastic instabilities of square cylinders. J. Sound Vib. **92**. 117–141 (1984). https://doi.org/10.1016/0022-460X(84)90378-X

Bai H, Mahbub Alam M.: Dependence of square cylinder wake on reynolds number. Phys. Fluids. **30**. 015102–119 (2018). https://doi.org/10.1063/1.4996945

Carassale L, Freda A, Marrè-Brunenghi M.: Effects of free-stream turbulence and corner shape on the galloping instability of square cylinders. J. Wind Eng. Ind. Aerodyn. **123**. 274–280 (2013). https://doi.org/10.1016/j.jweia.2013.09.002

Carassale L, Freda A, Marrè-Brunenghi M.: Experimental investigation on the aerodynamic behavior of square cylinders with rounded corners. J. Fluid Struct. **44**. 195–204 (2014). https://doi.org/10.1016/j.jfluidstructs.2013.10.010

Du X, Chen R, Ma W, Xu H, Zhao Y.: Aerodynamic characteristics of two closely spaced square cylinders in different arrangements. J. Wind Eng. Ind. Aerod. **208**. 104462–19 (2021). https://doi.org/10.1016/j.jweia.2020.104462

Du X, Chen R, Xu H, Ma W.: Experimental study on aerodynamic characteristics of two tandem square cylinders. Fluid Dynam. Res. **51**. 055508 (2019a). https://doi.org/10.1088/1873-7005/ab37b3

Datta B, Dey P, Das AK, Debbarma D.: Numerical analysis of fluid forces and heat transfer characteristics around tandem rounded corners square cylinders. J. Eng. Res. Appl. **9**. 40–51 (2019). https://doi.org/10.9790/9622-0906014051

Den Hartog JP.: Transmission line vibration due to sleet. Trans. Am. Inst. Electr. Eng. **51**(4), 1074–1076 (1932). https://doi.org/10.1109/T-AIEE.1932.5056223

Delany NK, Sorensen NE.: Low speed drag of cylinders of various shapes. Nat. Adv. Comm. Aero. Technical Note (1953). Technical Report 3038

Du X, Xu H, Ma W, Dai C, Liu Q.: Experimental study on aerodynamic characteristics of two square cylinders at various incidence angles. J. Wind Eng. Ind. Aerod. **191**. 154–169 (2019b). https://doi.org/10.1016/j.jweia.2019.05.019

Glauert H.: The rotation of an aerofoil about a fixed axis. Technical Report 595, Nat. Adv. Comm. Aero. Technical Note (1919)

Hu JC, Zhou Y, Dalton C.: Effects of corner radius on the near wake of a square prism. Exp. Fluids. **40**. 106–118 (2006). https://doi.org/10.1007/s00348-005-0052-2

Igarashi T.: Characteristics of the flow around two circular cylinders arranged in tandem: 1st report. Bull. JSME. **24**. 323–331 (1981). https://doi.org/10.1299/jsme1958.24.323

Igarashi T.: Characteristics of the flow around two circular cylinders arranged in tandem: 2nd report, unique phenomenon at small spacing. Bull. JSME. **27**. 2380–2387 (1984). https://doi.org/10.1299/jsme1958.27.2380

James WD, Vogel JM: Variation of section drag coefficient with variation of reynolds number for square cylinders with various corner radii. Technical report, Report for Valmont Industries (1996)

Letchford C, Mason M: Drag of square section tubes. Paper presented at the 13th Int. Conf. Wind Eng., Amsterdam, the Netherlands, 10–15 July 2011 (2011)

Mutlu Sumer B, Fredsøe J.: Hydrodynamics Around Cylindrical Structures. revised Edition. World Scientific Publishing Co. Pte. Ltd, Singapore (2006)

Niemann H-J, Hölscher N.: A review of recent experiments on the flow past circular cylinders. J. Wind Eng. Ind. Aerod. **33**. 197–209 (1990). https://doi.org/10.1016/0167-6105(90)90035-B

Okajima A.: Flow around two tandem circular cylinders at very high reynolds numbers. Bull. JSME. **22**. 504–511 (1979). https://doi.org/10.1299/jsme1958.22.504

Pearcy HH, Cash RF, Salter IJ, Boribond A: Interference effects on the drag loading for groups of cylinders in uni-directional flow. Technical Report R130, Nat. Maritime Inst. Rep. (1982)

Polhamus EC.: Effect of flow incidence and reynolds number on low-speed aerodynamic characteristics of several noncircular cylinders with applications to directional stability and spinning. Nat. Adv. Comm. Aero. Technical Note (1958). Technical Report 4176

Roshko A.: Experiments on the flow past a circular cylinder at very high reynolds numbers. J. Fluid Mech. **10**. 345–356 (1961). https://doi.org/10.1017/S0022112061000950

Reinhold TA, Tieleman HW, Maher FJ.: Interaction of square prisms in two flow fields. J. Wind Eng. Ind. Aerodyn. **2**. 223–241 (1977). https://doi.org/10.1016/0167-6105(77)90024-1

Schewe G.: On the force fluctuations acting on a circular cylinder in crossflow from subcritical up to transcritical reynolds numbers. J. Fluid Mech. **133**. 265–285 (1983). https://doi.org/10.1017/S0022112083001913

Sakamoto H, Haniu H, Obata Y.: Fluctuating forces acting on two square prisms in a tandem arrangement. J. Wind Eng. Ind. Aerodyn. **26**. 85–103 (1987). https://doi.org/10.1016/0167-6105(87)90037-7

Schewe G, Jacobs M.: Experiments on the flow around two tandem circular cylinders from sub- up to transcritical reynolds numbers. J. Fluids Struct. **88**. 148–166 (2019). https://doi.org/10.1016/j.jfluidstructs.2019.05.001

Sohankar A.: A numerical investigation of the flow over a pair of identical square cylinders in a tandem arrangement. Int. J. Numer. Methods Fluids. **70**. 1244–1257 (2012). https://doi.org/10.1002/fld.2739

Sohankar A.: A les study of the flow interference between tandem square cylinder pairs. Theor. Comput. Fluid Dyn. **28**. 531–548 (2014). https://doi.org/10.1007/s00162-014-0329-2

Schewe G, Van Hinsberg NP, Jacobs M.: Investigation of the steady and unsteady forces acting on a pair of circular cylinders in crossflow up to ultra-high reynolds numbers. Exp. Fluids. **62**. 176–194 (2021). https://doi.org/10.1007/s00348-021-03268-7

Tamura T, Miyagi T.: The effect of turbulence on aerodynamic forces on a square cylinder with various corner shapes. J. Wind Eng. Ind. Aerodyn. **83**. 135–145 (1999). https://doi.org/10.1016/S0167-6105(99)00067-7

Tamura T, Miyagi T, Kitagishi T.: Numerical prediction of unsteady pressures on a square cylinder with various corner shapes. J. Wind Eng. Ind. Aerodyn. **74–76**. 531–542 (1998). https://doi.org/10.1016/S0167-6105(98)00048-8

Van Hinsberg NP.: Mean and unsteady loading on square prisms with rounded edges: hard marine growth, incidence, and reynolds number effects. Mar. Struct. **75**. 102886–120 (2021a). https://doi.org/10.1016/j.marstruc.2020.102886

Van Hinsberg NP.: Aerodynamics of smooth and rough square-section prisms at incidence in very high reynolds-number cross-flows. Exp. Fluids. **62**(50), 1–17 (2021b). https://doi.org/10.1007/s00348-021-03143-5

Van Hinsberg NP.: The reynolds number dependency of the steady and unsteady loading on a slightly rough circular cylinder: from subcritical up to high transcritical flow state. J. Fluid Struct. **55**. 526–539 (2015). https://doi.org/10.1016/j.jfluidstructs.2015.04.002

Van Hinsberg NP.: Two identical tandem square prisms with rounded edges and hard marine fouling at incidence in crossflow: effect of spacing and reynolds number on unsteady fluid dynamics. Ocean Eng. **262**. 112302–132 (2022). https://doi.org/10.1016/j.oceaneng.2022.112302

Van Hinsberg NP.:High reynolds-number flows over bluff bodies. (2024). https://doi.org/10.15488/17984

Van Hinsberg NP, Frede A.: Square-section prism with rounded edges in a uniform cross-flow: effect of incidence angle and reynolds number on the (un)steady aerodynamics and proneness to galloping. J. Wind Eng. Ind. Aerodyn. **257**. 1–18 (2025). https://doi.org/10.1016/j.jweia.2024.105993

Van Hinsberg NP, Schewe G, Jacobs M.: Experiments on the aerodynamic behaviour of square cylinders with rounded corners at reynolds numbers up to 12 million. J. Fluid Struct. **74**. 214–233 (2017). https://doi.org/10.1016/j.jfluidstructs.2017.08.002

Van Hinsberg NP, Schewe G, Jacobs M.: Experimental investigation on the combined effects of surface roughness and corner radius for square cylinders at high reynolds numbers up to 10^7. J. Wind Eng. Ind. Aerodyn. **173**. 14–27 (2018). https://doi.org/10.1016/j.jweia.2017.12.003

Virkam CK, Ravindra HV, Krishne Gowda YT.: Visualisation of flow past square cylinders with corner modification. J. Mech. Energy Eng. **4**. 285–294 (2020). https://doi.org/10.30464/jmee.2020.4.3.285

Williamson CHK.: Vortex dynamics in the cylinder wake. Annu. Rev. Fluid Mech. **28**. 477–539 (1996). https://doi.org/10.1146/annurev.fl.28.010196.002401

Zhang W, Chen X, Yang H, Liang H, Wei Y.: Forced convection for flow across two tandem cylinders with rounded corners in a channel. Int. J. Heat Mass Transf. **130**. 1053–1069 (2019). https://doi.org/10.1016/j.ijheatmasstransfer.2018.10.125

Zdravkovich MM.: The effects of interference between circular cylinders in cross flow. J. Fluids Struct. **1**. 239–261 (1987). https://doi.org/10.1016/S0889-9746(87)90355-0

Zdravkovich MM: Flow Around Circular Cylinders. Vol 1: fundamentals. Oxford University Press, Oxford (1997)

Zhou Y, Yiu MW.: Flow structure, momentum and heat transport in a two-tandem-cylinder wake. J. Fluid Mech. **548**. 17–48 (2006). https://doi.org/10.1017/S002211200500738X